

1 Local wind regime induced by giant linear dunes:
2 comparison of ERA5-Land ~~re-analysis~~ reanalysis
3 with surface measurements

4 Cyril Gadal · Pauline Delorme ·
5 Clément Narteau · Giles F.S. Wiggs ·
6 Matthew Baddock · Joanna M. Nield ·
7 Philippe Claudin

8
9 Received: DD Month YEAR / Accepted: DD Month YEAR

10 **Abstract**

11 Emergence and growth of sand dunes results from the dynamic interaction
12 between topography, wind flow and sediment transport. While feedbacks be-
13 tween these variables are well studied at the scale of a single ~~and relatively~~
14 ~~small~~ dune, the average effect of a periodic ~~large-scale~~ dune pattern on atmo-
15 ~~small~~ atmospheric flows remains poorly constrained, due to a lack of data in major sand
16 seas. Here, we compare ~~field-local~~ measurements of surface ~~wind-data-winds~~
17 to the predictions of the ERA5-Land climate reanalysis at four locations in
18 Namibia, ~~including within the giant-dune within and outside the giant linear~~
19 ~~dune~~ field of the Namib sand sea. In the desert plains to the north of the sand
20 sea, observations and predictions agree well. This is also the case in the inter-
21 dune areas of the sand sea, ~~except for the weak winds blowing at night, which~~
22 ~~exhibit additional components during the day. During the night, however, an~~

C. Gadal

Institut de Mécanique des Fluides de Toulouse, Université de Toulouse Paul Sabatier, CNRS,
Toulouse INP-ENSEEIHT, Toulouse, France. E-mail: cyril.gadal@imft.fr

P. Delorme

Energy and Environment Institute, University of Hull, Hull, UK.

C. Narteau

Institut de Physique du Globe de Paris, Université de Paris, CNRS, Paris, France.

G. Wiggs

School of Geography and the Environment, University of Oxford, Oxford, UK.

M. Baddock

Geography and Environment, Loughborough University, Loughborough, UK.

J.M. Nield

School of Geography and Environmental Science, University of Southampton, Southampton,
UK.

P. Claudin

Physique et Mécanique des Milieux Hétérogènes, CNRS, ESPCI Paris, PSL Research Uni-
versity, Université de Paris, Sorbonne Université, Paris, France.

23 additional wind component aligned with the giant dune orientation, which
24 are not measured, in contrast to the easterly wind predicted by the ERA5-
25 Land reanalysis. We quantify these similarities and differences and provide a
26 physical understanding of the relevant aerodynamical regimes to relate them
27 link these discrepancies, with wind deviation and velocity attenuation larger
28 than 50° and 60 %, to the daily cycle of the turbulent atmospheric boundary
29 layer over a dune pattern of given wavelength. We conclude by identifying the
30 conditions under which the ERA5 Land reanalysis data can reliably be used
31 to study dune morphodynamics. We also propose that, in multidirectional
32 wind regimes, deflections of specific winds by complex topography, and to the
33 associated flow regimes. During the night, a shallow boundary layer induces a
34 flow confinement associated with a strong streamline compression above the
35 giant dunes, resulting in large flow deviations, especially for the lower
36 winds. During the day, the flow confinement is reduced by a thicker boundary
37 layer and higher wind velocities, and the feedback of the giant dunes on the
38 atmospheric flow is negligible. We finally propose that this mechanism and the
39 resulting wind deflections by the giant dunes could explain the occurrence of
40 smaller-scale secondary dune patterns with elongating along a different orienta-
41 tion compared to the primary structures between which they develop.

42 **Keywords** Atmospheric boundary layer · Sand dunes · Flow over hills

43 1 Introduction

44 The description of turbulent flows over complex topography is relevant for a
45 large variety of different environmental systems (Finnigan et al. 2020)(Sherman 1978; Walmsley et al. 1982; Baines 1995;
46 . For example, the flow over hills is of primary interest for wind power, me-
47 teorological and air pollution phenomena (Taylor et al. 1987). The prop-
48 erties of these flows are also key to the understanding of geophysical phe-
49 nomena, including the formation of wind-driven waves on the ocean surface
50 (Sullivan and McWilliams 2010), dissolution bedforms (Claudin et al. 2017)
51 (Claudin et al. 2017; Guérin et al. 2020), or sedimentary ripples and dunes
52 (Charru et al. 2013; Courrech du Pont 2015)(Bagnold 1941; Charru et al. 2013; Courrech du Pont 2015)
53 . Importantly, the troposphere presents a vertical structure, with a lower con-
54 vective boundary layer, of typical kilometer-scale thickness, capped by a stably
55 stratified region (Stull 1988). The largest topographic obstacles, such as moun-
56 tains, can therefore interact with this upper region and lead to internal wave
57 generation or significant wind disturbances, such as lee-side downslope winds
58 (Durran 1990).

59 ~~Focusing on the wind close to the surface, two related~~ Compared to hills and
60 ~~mountains, aeolian sand dunes offer idealized elevation profiles for the study~~
61 ~~of atmospheric turbulent flow over topographies, due to their smooth shape,~~
62 ~~free of canopies. Besides, dunes provide a rather wide range of scales, from~~
63 ~~decameters to kilometers, and very often come in a fairly regular pattern, which~~
64 ~~further simplifies the flow structure analysis. Past studies have highlighted~~
65 ~~two important topographic feedbacks on the windflow over dunes can be~~
66 ~~commented on separately~~
wind flow close to the dune/hill surface. First is the
67 effect on wind speed, with documented flow acceleration on upwind slopes
68 (Weaver and Wiggs 2011) and deceleration on downwind slopes (Baddock et al.
69 2007), where the speed-up factor is essentially proportional to the obstacle as-
70 pect ratio (Jackson and Hunt 1975). Importantly, the velocity maximum is typ-
71 ically shifted upwind of the obstacle crest (Jackson and Hunt 1975; Claudin et al. 2013)
72 . This behaviour has been theoretically predicted by means of asymptotic anal-
73 ysis of a neutrally stratified boundary-layer flow over an obstacle of vanishing
74 aspect ratio (Jackson and Hunt 1975; Mason and Sykes 1979; Sykes 1980; Hunt et al. 1988; Belcher and J.C.R. 1998)
75 (Jackson and Hunt 1975; Mason and Sykes 1979; Sykes 1980; Hunt et al. 1988; Belcher and J.C.R. 1998; Kroy et al. 2000)
76 . Experiments in flumes (Zilker et al. 1977; Zilker and Hanratty 1979; Fred-
77 erick and Hanratty 1988; Poggi et al. 2007; Bristow et al. 2022), in wind
78 tunnels (Gong and Ibbetson 1989; Finnigan et al. 1990; Gong et al. 1996)
79 and in field conditions at all scales (Taylor and Teunissen 1987; Claudin et al.
80 2013; Fernando et al. 2019; Lü et al. 2021), have also documented this ef-
81 fect. Interestingly, a similar behaviour exists for the pressure perturbation,
82 but with a slight downwind shift for the pressure minimum (Claudin et al.
83 2021). The second effect, much less studied, is the flow deflection that oc-
84 curs when the incident wind direction is not perpendicular to the ridge crest.
85 While predicted to be small (less than 10°) in the linear regime valid for
86 shallow topography (Gadal et al. 2019), significant flow steering has been
87 reported in the field on the downwind side of steep enough obstacles, such

as mountain ranges (Kim et al. 2000; Lewis et al. 2008; Fernando et al. 2019), well-developed sand dunes (Walker et al. 2009; Hesp et al. 2015; Walker et al. 2017; Smith et al. 2017; de Winter et al. (Tsoar and Yaalon 1983; Sweet and Kocurek 1990; Walker and Nickling 2002; Smith et al. 2017) and in particular coastal foredunes (e.g. Hunter et al. (1983), Rasmussen (1989), Walker et al. (2006), Walker et al. (2009), Hesp et al. (2015), Walker et al. (2017), de Winter et al. (2020)), mountain ranges (Kim et al. 2000; Lewis et al. 2008; Fernando et al. 2019), and valley topographies (Wiggs et al. 2002; Garvey et al. 2005).

For practical reasons, wind measurement Wind measurements over sand dunes has been mainly performed over small bedforms, typically a few meters high (corresponding to several tens of meters long) (e.g. Mulligan (1988), Hesp et al. (1989), Lancaster et al. (1996), Mckenna Neuman et al. (1997), Sauermann et al. (2003), Andreotti et al. (2002), Walker and Nickling (2002), Weaver and Wiggs (2011)). Giant dunes For practical reasons, fewer studies performed similar measurements on giant dunes (Hayholm and Kocurek 1988), with kilometer-scale wavelengths and heights of tens of meters, are more difficult to investigate although for several reasons they. However, such large dunes provide a choice configuration for the study of turbulent flows over a complex topography. First, one expects larger wind disturbances for larger obstacles. Secondly, their large size makes can make them interact with the vertical structure of the atmosphere (Andreotti et al. 2009). Third, they usually form large patterns in sand seas and thus behave as rather clean periodic perturbations, in contrast with isolated dunes. Finally, because the morphodynamics of aeolian bedforms are is strongly dependent on the local wind regime (Livingstone and Warren 2019), one can expect to see the consequences of windflow disturbance by large dunes on neighbouring small dunes (Brookfield 1977; Ewing et al. 2006). A similar effect is observed on the properties of impact ripple patterns due to the presence of dunes (Howard 1977; Hood et al. 2021) (Howard 1977; Hood et al. 2021).

Atmospheric flows have been much studied at the desert-scale with climate reanalyses based on global atmospheric models (Blumberg and Greeley 1996; Livingstone et al. 2010; Ashkenazy et al. 2012; Blumberg and Greeley 1996; Livingstone et al. 2010; Ashkenazy et al. 2012; Jolivet et al. 2021; Hu et al. 2021; Gunn et al. 2021), such as ERA-40, ERA-Interim or ERA-5 ERA5 (Uppala et al. 2005; Dee et al. 2011; Hersbach et al. 2020). However, the spatial resolution of these reanalyses (tens of kilometers) of these reanalyses implies average quantities that do not resolve the smaller scales of interest, which range from individual dunes to small mountains (Livingstone et al. 2010). Recently, the release of ERA5-Land has partly resolved this limitation by providing up to 70 years of hourly wind predictions at a 9 km spatial resolution (Muñoz-Sabater et al. 2021). However, its validity remains to be studied, especially in remote desert areas where assimilation of measured data is very low.

In this work, we compare local wind speeds and directions measured by meteorological stations at four different locations inside and north of the giant-dune giant linear dune field of the Namib sand sea to the regional predictions of the ERA5-Land climate reanalysis. Where the meteorological stations are surrounded by a relatively flat environment, we show that local measurements and regional predictions agree well. The agreement is also good in the

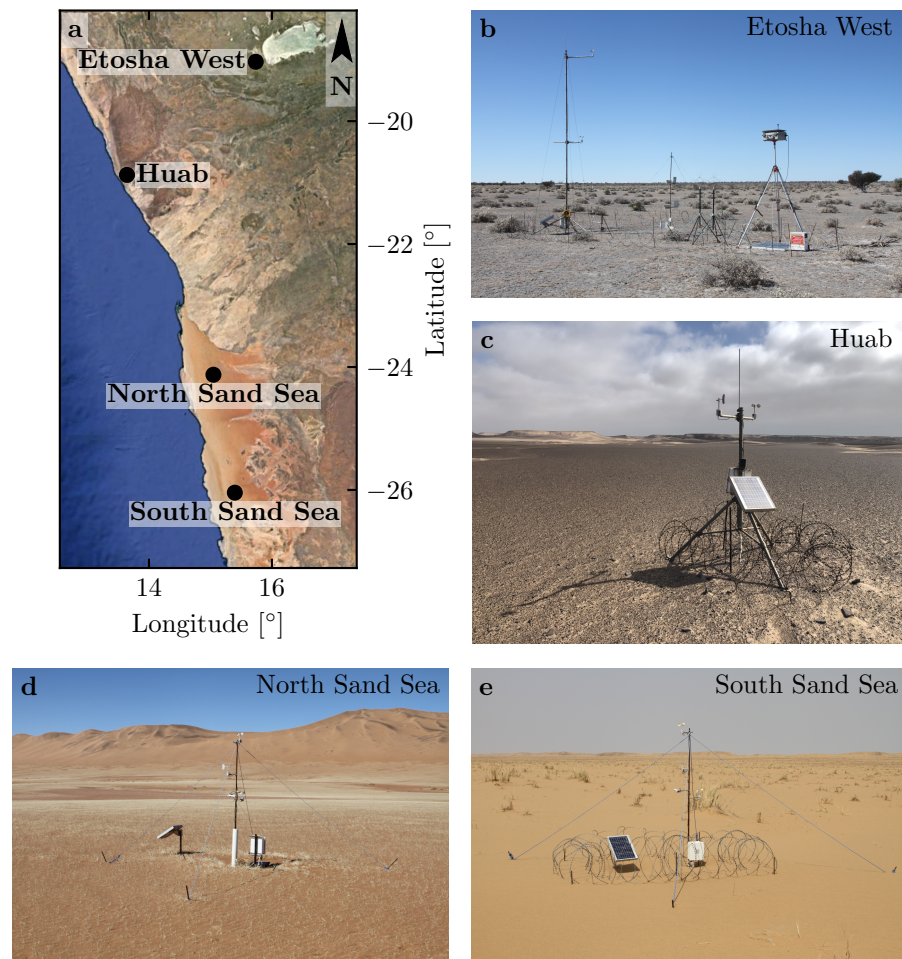


Fig. 1 Studied field sites. **a:** Location of the different sites in Namibia. **b–e:** Photographs of the meteorological stations.

134 interdune areas of the sand sea, except for some weak winds blowing at night,
 135 which exhibit an additional component aligned with the giant dune orientation.
 136 These winds are not predicted by the ERA5-Land reanalysis (section 2).
 137 Further, we are able to link the magnitude of these differences to the circadian
 138 cycle of the atmospheric boundary layer (section 3). Finally, we draw implica-
 139 tions for the wind disturbances on smaller-scale dunes (section 4), suggesting
 140 a possible origin for crossing dunes.

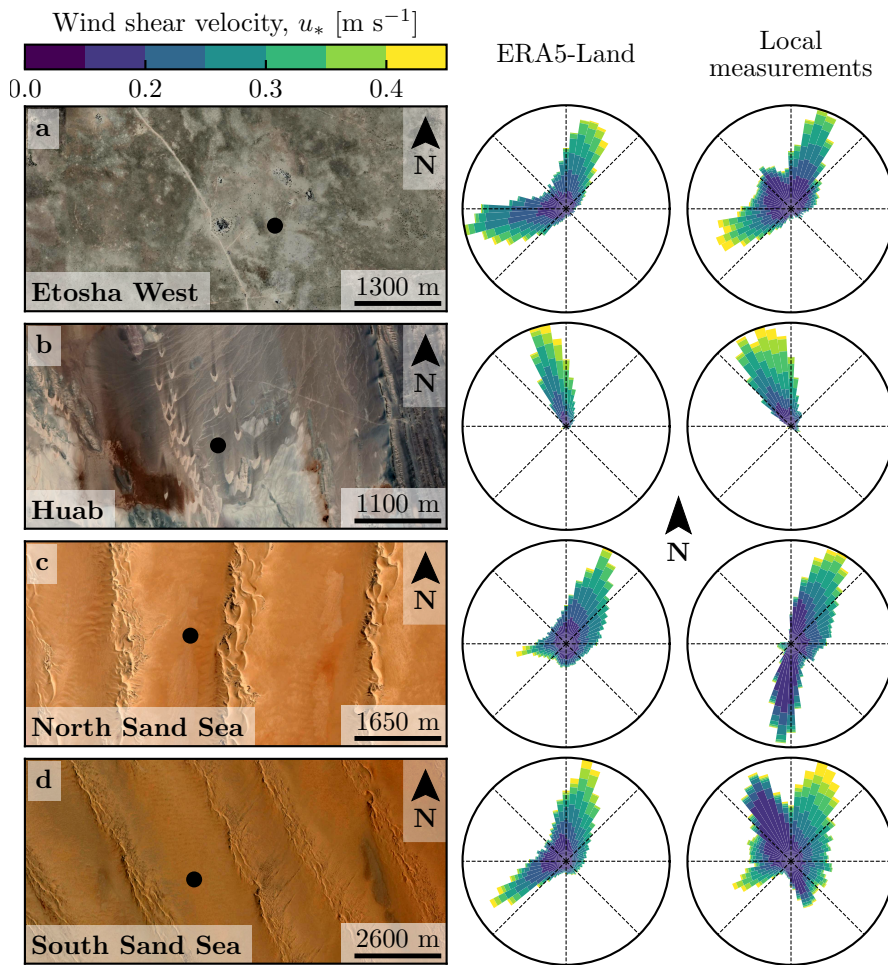


Fig. 2 Wind data used in this study. Satellite images of ~~these~~ the different environments (Google-Earth, Maxar Technologies, CNES/Airbus) are shown on the left. The black dots show the location of the wind measurement stations. On the ~~center and on-the-right of the photos, the corresponding~~ wind roses representing the data from the ERA5-Land climate reanalysis and the local wind stations are ~~respectively shown~~ displayed. Note: ~~the graphical convention for the wind roses is~~ that the bars show the direction towards which the wind blows (see color bar for velocity scale).

141 2 Wind regimes across the Namib Sand Sea

142 We measured the wind regime at four different locations in Namibia, representative
 143 of various arid environments across the Namib desert (Fig. 1, Fig. 2).
 144 The Etosha West station was located at the Adamax waterhole to the west
 145 of Etosha Pan in northern Namibia, in a sparsely vegetated area. The Huab
 146 station was near the coast on a hyper-arid flat gravel plain lying north the

147 ephemeral Huab river. Here, barchan dunes up to a few meters in height de-
148 velop from the sediment blowing out of the river valley (Nield et al. 2017;
149 Hesp and Hastings 1998). These two stations were both located in relatively
150 flat environments. In contrast, the North Sand Sea and South Sand Sea sta-
151 tions were located in the interdunes between linear dunes with kilometer-scale
152 wavelengths, hectometer-scale heights and superimposed patterns. In this sec-
153 tion, we describe and compare winds from local measurements and climate
154 reanalysis predictions.

155 2.1 Wind and elevation data

156 At each meteorological station (Fig. 1), wind speed and direction were sampled
157 every 10 minutes using cup anemometers (Vector Instruments A100-LK) and
158 wind vanes (Vector Instruments W200-P) at ~~heights which varied a single~~
159 height, which was between 2 m and 3 m depending on the station. The available
160 period of measurements at each station ranged from 1 to 5 discontinuous years
161 distributed between 2012 and 2020 (Online Resource Fig. S1). We checked that
162 at least one complete seasonal cycle was available for each station. Regional
163 winds were extracted at the same locations and periods from the ERA5-Land
164 dataset, which is a replay at a smaller spatial resolution of ERA5, the latest
165 climate reanalysis from the ECMWF (Hersbach et al. 2020; Muñoz-Sabater
166 et al. 2021). This dataset provided hourly predictions of the 10-m wind velocity
167 and direction at a spatial resolution of $0.1^\circ \times 0.1^\circ$ (≈ 9 km in Namibia).

168 To enable direct comparison, the local wind measurements were averaged
169 into 1-hr bins centered on the temporal scale of the ERA5-Land estimates
170 (Online Resource Fig. S2). As the wind velocities of both datasets were pro-
171 vided at different heights, we converted them into shear velocities u_* (Online
172 Resource section 1), characteristic of the turbulent wind profile. Wind roses
173 in Fig. 2 show the resulting wind data.

174 Dune properties were computed using autocorrelation on the 30-m Digital
175 Elevation Models (DEMs) of the shuttle radar topography mission (Farr et al.
176 2007). For the North and South Sand Sea stations, we obtain, respectively,
177 orientations of 85° and 125° with respect to the North, wavelengths of 2.6 km
178 and 2.3 km and amplitudes (or half-heights) of 45 m and 20 m (Online Resource
179 Fig. S4 for more details). This agrees with direct measurements made on site.

180 2.2 Comparison of local and regional winds

181 The measured and predicted wind regimes are shown in Fig. 2. In the Namib,
182 the regional wind patterns are essentially controlled by the sea breeze, result-
183 ing in strong northward components (sometimes slightly deviated by the large
184 scale topography) present in all regional wind roses (Lancaster 1985). These
185 daytime winds are dominant during the period October-March (Fig. 3f and
186 Online Resource Fig. 4f). During April-September, an additional (and often

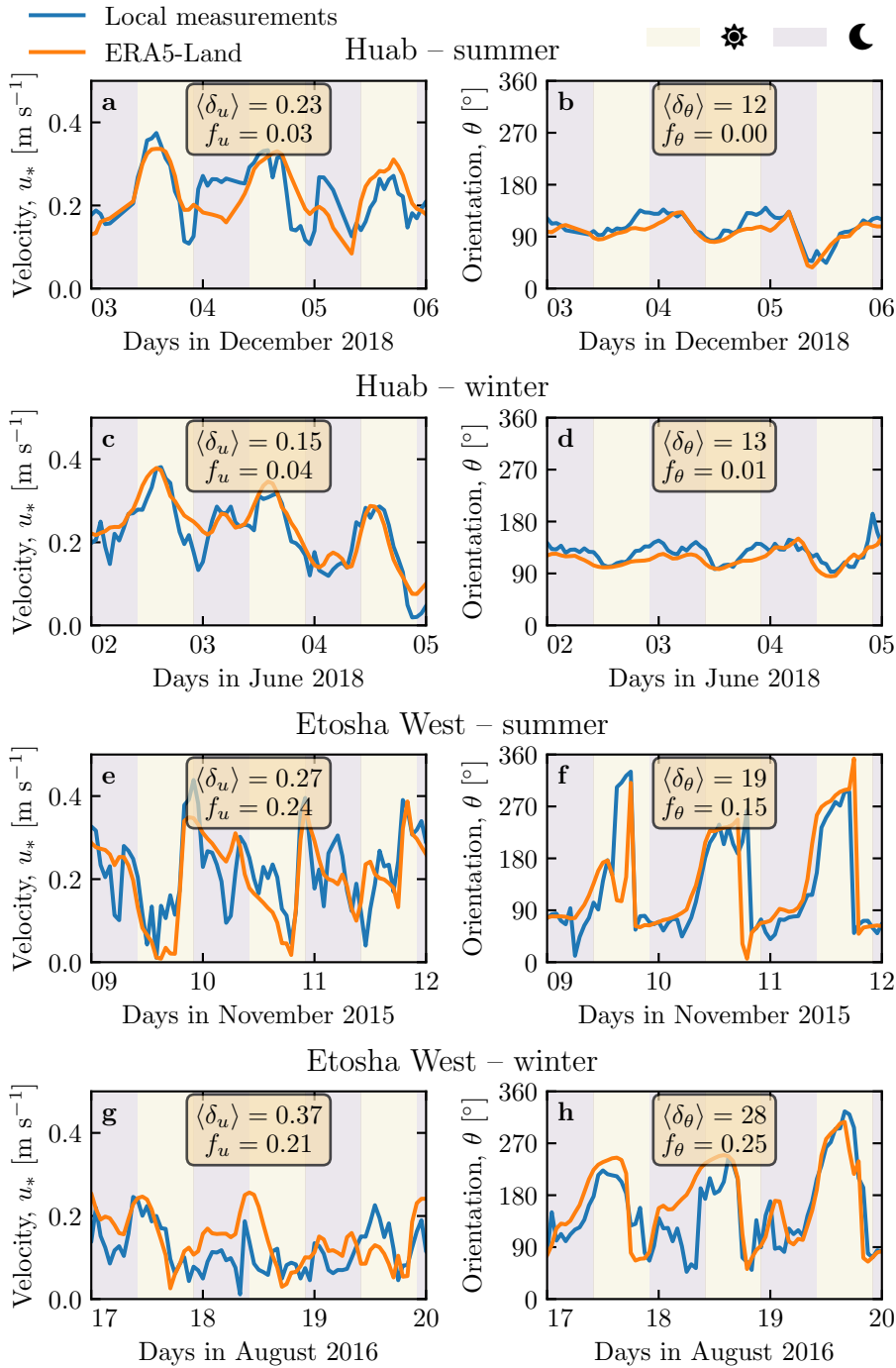


Fig. 3 Temporal comparison between the wind data coming from the ERA5-Land climate reanalysis (orange lines) and from the local measurements (blue lines). Coloured swathes indicate day (between 1000–10.00 UTC and 2200–22.00 UTC) and night (before 1000–10.00 UTC or after 2200–22.00 UTC). Numbers in legends indicate the average flow deflection δ_θ and relative wind modulation δ_u over the displayed period (see section 3.2 for their definitions), as well as the percentage f_θ and f_u of occurrence of extreme events ($\delta_\theta > 50^\circ$ and $|\delta_u| > 0.6$). **a–b:** Etosha West–Huab station in summer. **b–c:** Etosha West–Huab station in winter. **d–e:** Huab–Etosha West station in summer. **f–g:** Huab–Etosha West station in winter. Time series of the two other stations are shown in Fig. 5.

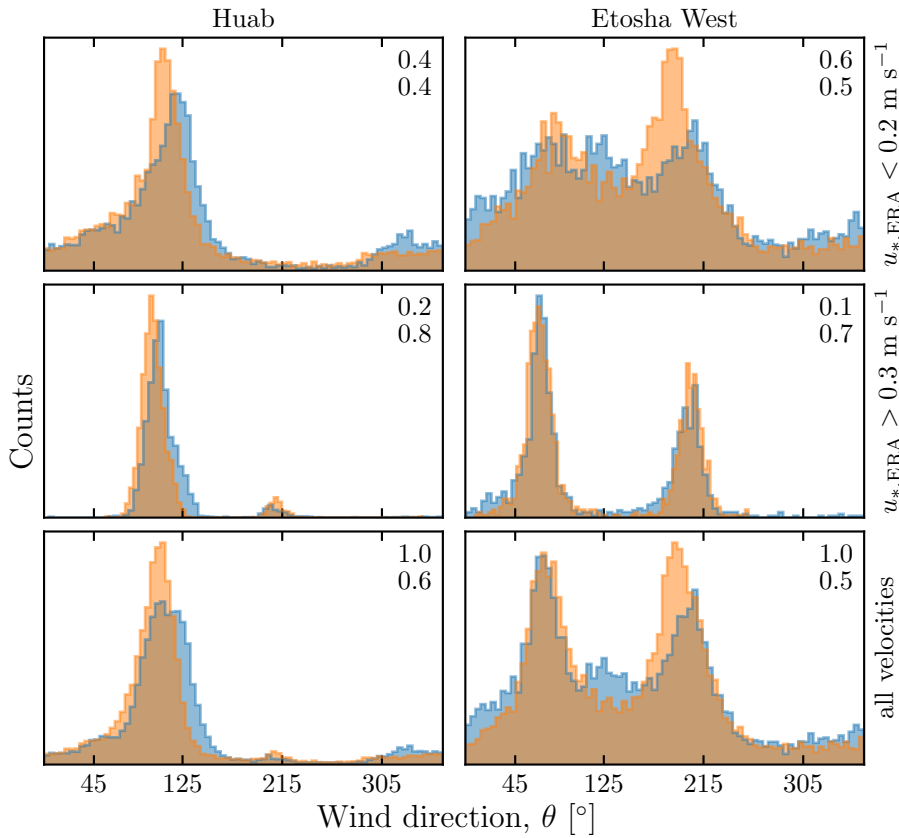


Fig. 4 Distributions of wind direction at the Huab and Etosha West stations for the ERA5-Land climate reanalysis (orange) and the local measurements (blue). In each subplot, both distributions are plotted from the same time steps, selected with constraints on for different ranges of the wind wind velocity (rows) in the ERA5-Land dataset. The numbers at the top centre upper right corners give the percentage of time steps selected in each sub-range (top), as well as the percentage of them corresponding to the day defined between 1000 10.00 UTC and 2200–22.00 UTC (bottom).

nocturnal) easterly component can also be recorded, induced by the combination of katabatic winds forming in the mountains, and infrequent ‘berg’ winds, which are responsible for the high wind velocities observed (Lancaster et al. 1984). The frequency of these easterly components decreases from inland to the coast. As a result, bidirectional wind regimes within the Namib Sand Sea and at the west Etosha site (Fig. 2a,c,d) and a unidirectional wind regime on the coast at the outlet of the Huab River (Fig. 2b) are observed.

In the case of the Etosha West and Huab stations, the time series of wind speed and direction from the regional predictions quantitatively match those corresponding to the local measurements (Figs. 3, 4 and Online Resource Fig. S5). For the North Sand Sea and South Sand Sea stations within the giant linear dune field, we observe that this agreement is also good, but limited to

199 the October-March time period (Fig. 4a, b, e, f). However, the field-measured
 200 wind roses exhibit additional wind components aligned with the ~~giant~~-dune
 201 orientation, as evidenced on the satellite images (Fig. 2c,d).

202 More precisely, during the April-September period, the local and regional
 203 winds in the interdune match during daytime only, i.e when the southerly/-
 204 southwesterly sea breeze dominates (Figs. 5c,d,g,h and 6). In the late after-
 205 noon and during the night, when the easterly ‘berg’ and katabatic winds blow,
 206 measurements and predictions differ. In this case, the angular wind distri-
 207 bution of the local measurements exhibits two additional modes correspond-
 208 ing to reversing winds aligned with the ~~giant~~-dune orientation (purple frame
 209 in Fig. 6, Online Resource Fig. S6). This deviation is also associated with
 210 a general attenuation of the wind strength (Online Resource Fig. S7). Re-
 211 markably, all these figures show that these wind reorientation and attenua-
 212 tion processes occur only at low velocities of the regional wind, typically for
 213 $u_{*,\text{ERA}} \lesssim 0.2 \text{ m s}^{-1}$ $u_{*,\text{ERA5-Land}} \lesssim 0.2 \text{ m s}^{-1}$. For shear velocities larger than
 214 $u_{*,\text{ERA}} \approx 0.3 \text{ m s}^{-1}$ $u_{*,\text{ERA5-Land}} \approx 0.3 \text{ m s}^{-1}$, the wind reorientation is not ap-
 215 parent. Finally, for intermediate shear velocities, both situations of wind flow
 216 reoriented along the dune crest and not reoriented can be successively ob-
 217 served (Online Resource Fig. S6). Importantly, these values are not precise
 218 thresholds (and certainly not related to the threshold for sediment transport),
 219 but indicative of a crossover between regimes, whose physical interpretation is
 220 discussed in the next section.

221 3 Influence of wind speed and circadian cycle on the atmospheric 222 boundary layer

223 The wind deflection induced by ~~linear~~-dunes has previously been related to the
 224 incident angle between wind direction and crest orientation, with a maximum
 225 deflection evident for incident angles between 30° and 70° (Walker et al. 2009;
 226 Hesp et al. 2015). In the data analysed here, the most deflected wind at both
 227 the North and South Sand Sea stations is seen to be where the incident angle
 228 is perpendicular to the giant dunes (Figs. 2 and 6). It therefore appears that
 229 in our case, the incident wind angle is not the dominant control on maximum
 230 wind deflection. Further, and as shown in Fig. 6, winds of high and low veloc-
 231 ities show contrasting behaviour in characteristics of deflection. This suggests
 232 a change in hydrodynamical regime between the winds. In this section, we
 233 discuss the relevant parameters associated with the dynamical mechanisms
 234 that govern the interactions between the atmospheric boundary layer flow and
 235 giant dune topographies. This analysis allows us to provide a physics-based
 236 interpretation of our measured wind data.

237 3.1 Flow over a modulated bed

238 Taking as a reference the turbulent flow over a flat bed, the general framework
 239 of our study is understanding and describing the flow response to a bed mod-

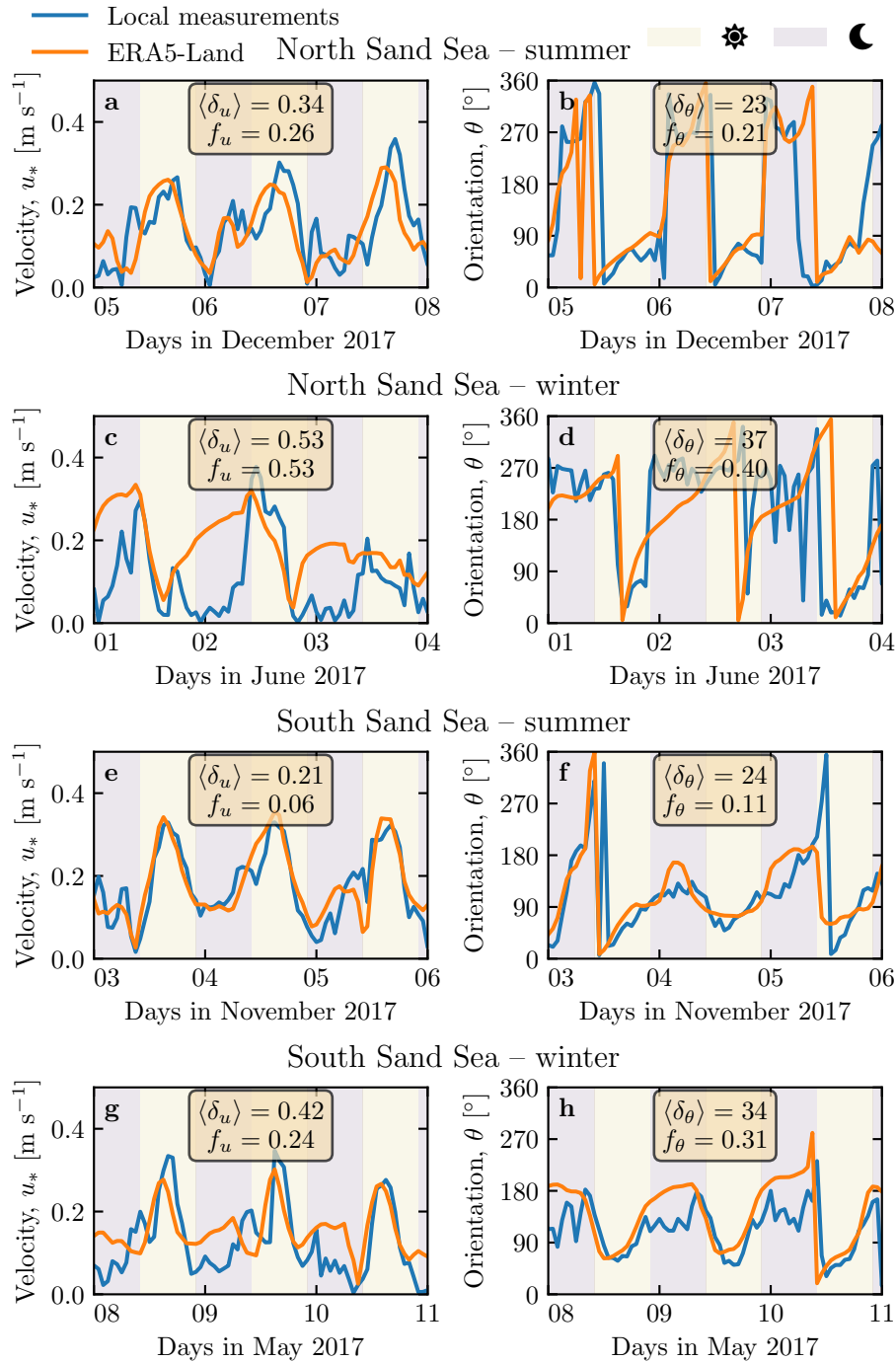


Fig. 5 Temporal comparison between the wind data coming from the ERA5-Land climate reanalysis (orange lines) and from the local measurements (blue lines). Same as Fig. Coloured swatches indicate day (between 1000 UTC and 2200 UTC) and night (before 1000 UTC or after 2200 UTC). **a–b:** North Sand Sea station in summer. **b–c:** (a–b), North Sand Sea station in winter. **d–e:** (b–c), South Sand Sea station in summer. **f–g:** (d–e) and South Sand Sea station in winter. Time series of the two other stations are shown in Fig. 3(f–g).

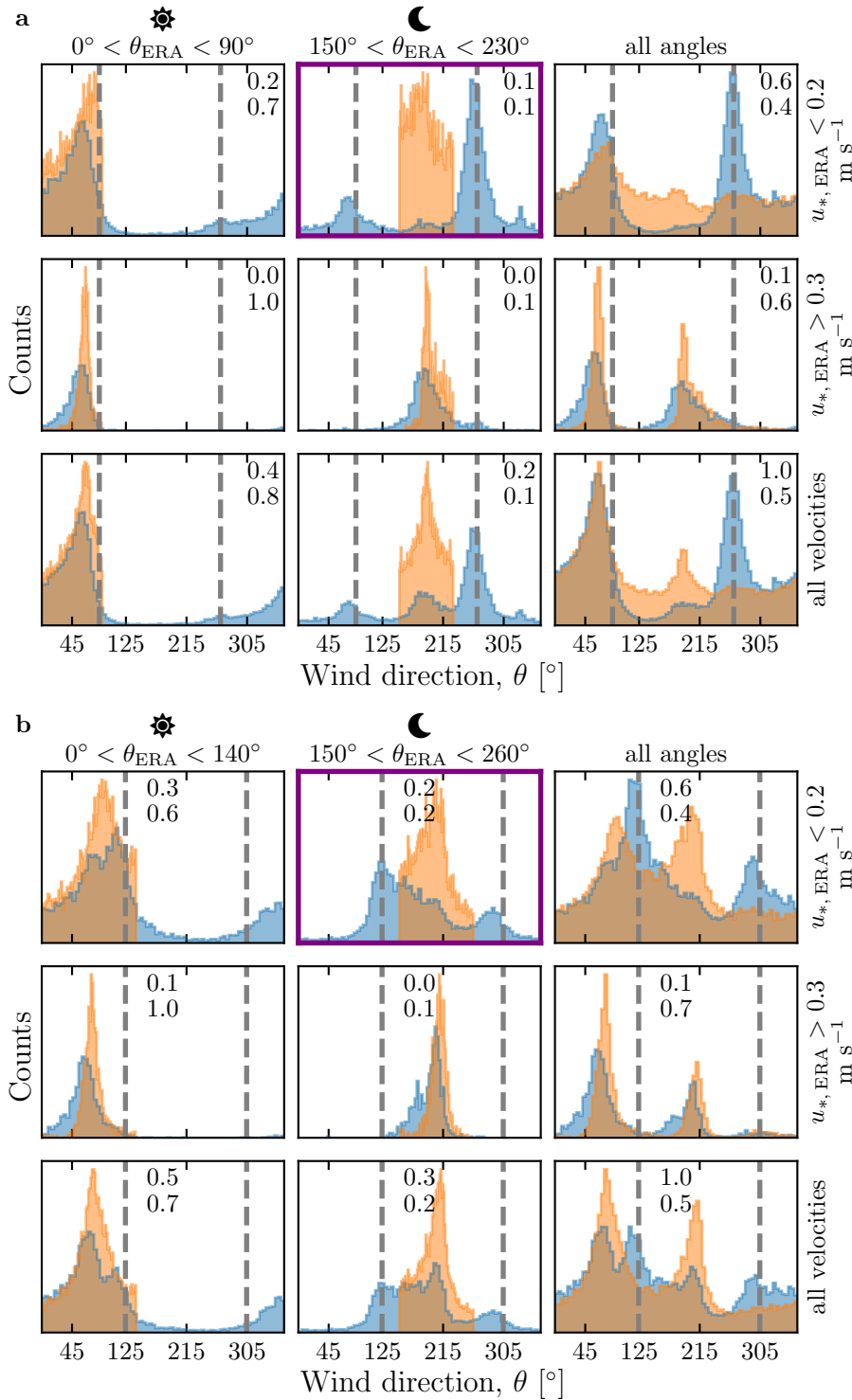


Fig. 6 Distributions of wind direction at the Same as Fig. 4 but for North Sand Sea (a) and South Sand Sea (b) stations for the ERA5-Land climate reanalysis (orange) and the local measurements (blue). In each subplot, both distributions are plotted from the same time steps. Here, selected with constraints on subplots correspond to different ranges for the wind direction (columns) and for wind velocity (rows) of the ERA5-Land dataset. The grey vertical dashed lines indicate the main dune orientation. The numbers in contrast with observations at the top right give the percentage of time steps selected in each sub-range, as well as the percentage corresponding to the daytime (between 1000 UTC and 2200 UTC). Contrary to the Huab and Etosha West stations (Fig. 4), histograms do not match well at low wind velocities. More specifically, and the purple frame highlights the regime (low wind velocities, nocturnal easterly wind) in which the data from both datasets differ most.

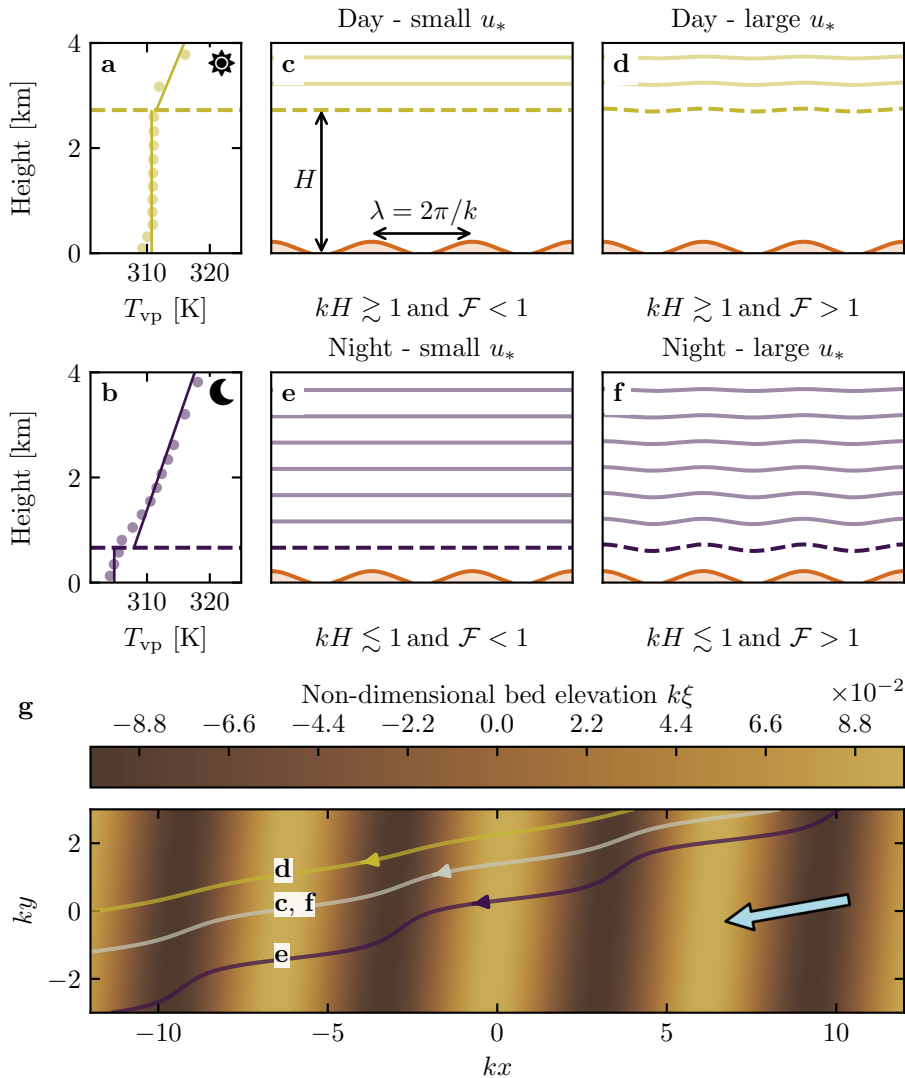


Fig. 7 **a–b:** Vertical profiles of the virtual potential temperature T_{vp} at **two** different time steps (day - 03/11/2015 - **1200-12.00** UTC, night - 01/13/2013 - **0900-09.00** UTC) at the North Sand Sea station. Dots: data from the ERA5 reanalysis. Dashed lines: boundary layer height given by the ERA5 reanalysis (Online Resource section 2). Plain lines: vertical (boundary layer) and linear (free atmosphere) fits to estimate the stratification properties. **c–f:** Sketches representing the interaction between the giant dunes and the atmospheric flow for different meteorological conditions. **g:** Streamlines over a sinusoidal topography $\xi(x, y)$ qualitatively representing the effect of low, medium and strong flow confinement, in relation to the above panels (see Appendix 1 for more details). The blue arrow indicates the undisturbed wind direction.

ulation (e.g. a giant dune). Without loss of generality, we can consider in this context an idealised bed elevation in the form of parallel sinusoidal ridges, with wavelength λ (or wavenumber $k = 2\pi/\lambda$) and amplitude ξ_0 , and where the reference flow direction makes a given incident angle with respect to the ridge crest (Andreotti et al. 2012). Part of this response, on which we focus here, is the flow deflection by the ridges. In a simplified way, it can be understood from the Bernoulli principle (Hesp et al. 2015): as the flow approaches the ridge crest, the compression of the streamlines results in larger flow velocities, and thus lower pressures ([Rubin and Hunter 1987](#)) ([Jackson and Hunt 1975](#)). An incident flow oblique to the ridge is then deflected towards lower pressure zones, i.e. towards the crest. Turbulent dissipation tends to increase this effect downstream, resulting in wind deflection along the crest in the lee side (Gadal et al. 2019).

Flow confinement below a capping surface, which enhances streamline compression, has a strong effect on the hydrodynamic response and typically increases flow deflection. This is the case for bedforms forming in open channel flows such as rivers ([Fourrière et al. 2010](#); [Unsworth et al. 2018](#)) ([Kennedy 1963](#); [Chang and Simons 1970](#); [Mizumura 1995](#)). This is also relevant for aeolian dunes as they evolve in the turbulent atmospheric boundary layer (ABL) capped by the stratified free atmosphere (FA) (Andreotti et al. 2009). Two main mechanisms, associated with dimensionless numbers must then be considered (Fig. 7). First, topographic obstacles typically disturb the flow over a characteristic height similar to their length. As flow confinement is characterised by a thickness H , the interaction between the dunes and the wind in the ABL is well captured by the parameter kH . The height H is directly related to the [radiative fluxes at sensitive heat flux from](#) the Earth surface. It is typically on the order of a kilometre, but significantly varies with the circadian and seasonal cycles. Emerging and small dunes, with wavelengths in the range 20 to 100 m, are not affected by the [flow](#) confinement, corresponding to $kH \gg 1$. For giant dunes with [kilometric kilometer-scale](#) wavelengths, however, their interaction with the FA [is-can be](#) significant (Andreotti et al. 2009). This translates into a parameter kH in the range 0.02–5, depending on the moment of the day and the season. A second important mechanism is associated with the existence of a thin intermediate so-called capping layer between the ABL and the FA. It is characterised by a density jump $\Delta\rho$, which controls the ‘rigidity’ of this interface, i.e. how much its deformation affects streamline compression. This is usually quantified using the Froude number (Vosper 2004; Stull 2006; Sheridan and Vosper 2006; Hunt et al. 2006; Jiang 2014):

$$\mathcal{F} = \frac{U}{\sqrt{\frac{\Delta\rho}{\rho_0} g H}}, \quad (1)$$

where U is the wind velocity at the top of the ABL and ρ_0 its average density. The intensity of the stratification, i.e. the amplitude of the gradient $|\partial_z \rho|$ [in the FA](#), also impacts [its-the](#) ability to deform the capping layer under the presence of an underlying obstacle, and thus affects the influence of flow

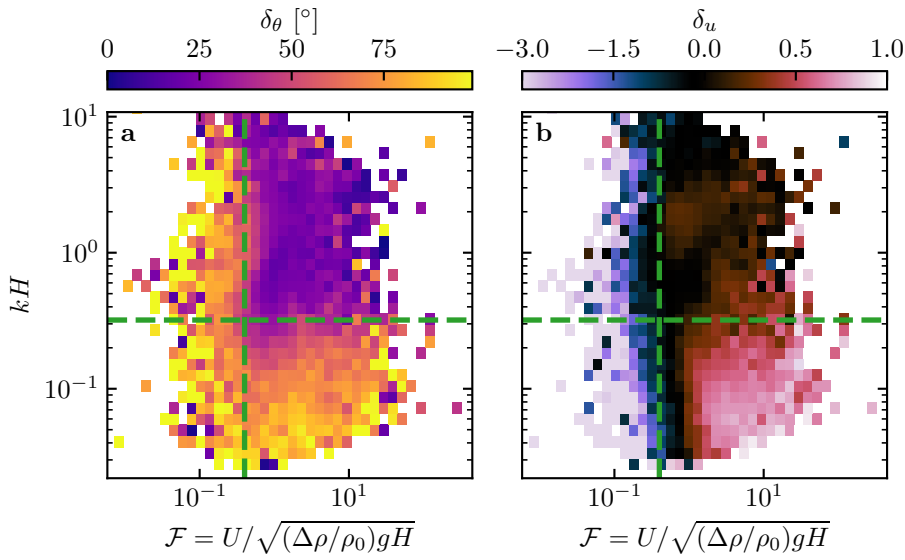


Fig. 8 Regime diagrams of the wind deviation δ_θ (a) and relative attenuation/amplification δ_u (b) in the space (\mathcal{F}, kH) , containing the data from both the North Sand Sea and South Sand Sea stations. **Green** The green dashed lines empirically delimit the different regimes. The point density in each bin of the diagrams is shown in Online Resource Fig. S10 – 95% of the data occur in the range $-1 < \delta u < 1$. Similar regime diagrams in the spaces (\mathcal{F}_I, kH) and $(\mathcal{F}_I, \mathcal{F})$ are shown in Online Resource Fig. S11.

confinement. This can be quantified using the internal Froude number (Vosper 2004; Stull 2006; Sheridan and Vosper 2006; Hunt et al. 2006; Jiang 2014) $\mathcal{F}_I = kU/N$, where $N = \sqrt{-g\partial_z\rho/\rho_0}$ is the Brunt-Väisälä frequency (Stull 1988). Both Froude numbers have in practice the same qualitative effect on flow confinement (a smaller Froude corresponding to a stiffer interface), and we shall restrict the main discussion to \mathcal{F} only.

With this theoretical framework in mind, and in the context of the measured wind data in the North and South Sand Sea stations, the smallest wind disturbances are expected to occur during the day, when the ABL depth is the largest and comparable to the dune wavelength ($kH \gtrsim 1$), which corresponds to a weak confinement situation (Fig. 7c,d). In contrast, large wind disturbances are expected to occur during the night, when the confinement is mainly induced by a shallow ABL (Fig. 7e). However, this strong confinement can be somewhat reduced in the case of strong winds, corresponding to large values of the Froude number and a less ‘rigid’ interface (Fig. 7f). This is in qualitative agreement with the transition from deflected to non-deflected winds related to low and high velocities observed in our data (Sec. 2.2).

299 3.2 Data distribution in the flow regimes

300 We can go one step further and analyse how our data quantitatively spread
 301 over the different regimes discussed above. For that purpose, one needs to
 302 compute kH and \mathcal{F} from the time series. H , U and the other atmospheric
 303 parameters can be deduced from the various vertical profiles (temperature,
 304 humidity) available in the ERA5 climate reanalysis (Online Resource section
 305 2). We quantify the flow deflection δ_θ as the minimal angle between the wind
 306 orientations comparing the local measurements and the regional predictions.
 307 We also compute the relative velocity modulation as

$$\delta_u = \frac{\frac{u_*^{\text{ERA}} - u_*^{\text{station}}}{u_*^{\text{ERA}}} \frac{u_*^{\text{ERA5-Land}} - u_*^{\text{Local mes.}}}{u_*^{\text{ERA5-Land}}}}{\frac{u_*^{\text{ERA}}}{u_*^{\text{ERA5-Land}}}}. \quad (2)$$

308 These two quantities are represented as maps in the plane (\mathcal{F} , kH) (Fig. 8a,b),
 309 and one can clearly identify different regions in these graphs. Small wind dis-
 310 turbances (small δ_θ and δ_u) are located in the top-right part of the diagrams,
 311 corresponding to a regime with low-interaction as well as low-confinement (kH
 312 and \mathcal{F} large enough, Fig. 7d). Lower values of kH (stronger interaction) or of
 313 Froude number (stronger confinement) both lead to an increase in wind dis-
 314 turbances, both in terms of orientation and velocity. Below a crossover value
 315 $kH \simeq 0.3$, wind disturbance is less sensitive to the \mathcal{F} -value. This is probably
 316 due to enhanced non-linear effects linked to flow modulation by the obstacle
 317 when confinement is strong (e.g. wakes and flow recirculations). The Froude
 318 number also controls a transition from damped to amplified wind velocities
 319 in the interdune, with a crossover around $\mathcal{F} \simeq 0.4$ (Fig. 8b). Such an ampli-
 320 fication is rather unexpected. Checking the occurrence of the corresponding
 321 data, it appears that these amplifications are associated with the southerly
 322 sea breeze, and occur dominantly during the October-March period, when the
 323 other easterly wind is not present (Online Resource Fig. S12a–b). Further-
 324 more, they occur less frequently during the afternoon, and more frequently
 325 at the end of the day (Online Resource Fig. S12c). This effect may be linked
 326 to a change in the flow behaviour in the lee side of the obstacles but further
 327 measurements are needed in order to assess the different possibilities (Baines
 328 1995; Vosper 2004).

329 It is important to discuss the sensitivity of the results with respect to
 330 the choice of the hydrodynamic roughnesses (see Online Resource section 4).
 331 In fact, the only quantities dependent on this choice are those which involve
 332 the amplitude of the velocities: wind shear velocities, Froude number \mathcal{F} and
 333 relative velocity modulation δ_u . Those associated with wind direction are
 334 independent of this choice. Considering the possible range of realistic roughnesses
 335 values, the uncertainty on velocities estimated using the law of the wall is at
 336 most 30%. A similar maximum uncertainty applies to the Froude number.
 337 This uncertainty also propagates to δ_u , for which Figure S14 shows that the
 338 choice of roughness has little influence of its temporal variations, even if it
 339 can induce a global increase or decrease of its values. As such, the choice

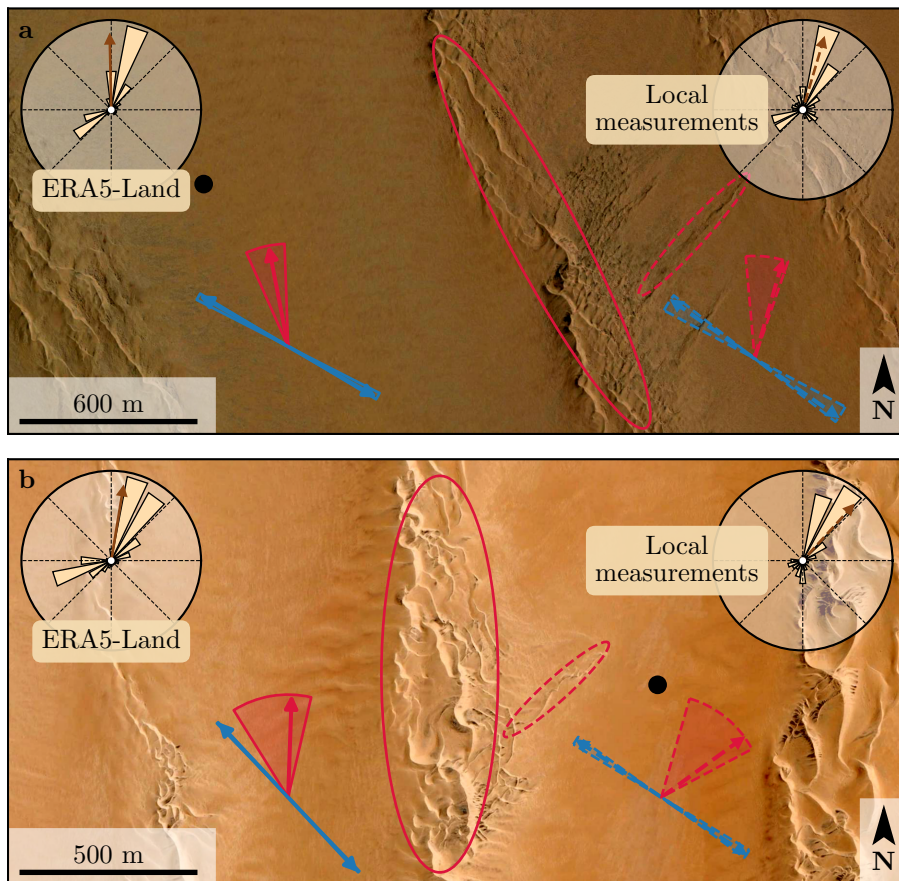


Fig. 9 Implications for smaller scale patterns in (a) the South Sand Sea and (b) North Sand Sea. The ellipses indicate the different types of elongating dunes, at large (plain line) and small (dashed line) scales. Dune orientation are predicted using the model of Courrech du Pont et al. (2014) from the sand flux angular distributions, shown here (roses and) along with the resultant transport direction (brown arrow) for typical values (grain size 180 μm , flux-up ratio of 1.6). Code for corresponding arrows: use of ERA5-Land data (plain line), use of local measurements (dashed line), prediction for the bed instability growth mechanism (blue), prediction for the elongation growth mechanism (red). Wedges show the uncertainty on the orientation calculation when parameters are varied. The black dots indicate the location of the meteorological stations with respect to in the dunes interdune. See Appendix 2 for additional details.

340 of z_0 will not qualitatively affect the overall aspect of the regime diagram
 341 presented in Figure 8b. It may only change the crossover value of δ_u at which
 342 the transition between regimes is observed (dashed green lines in that figure).
 343 Our conclusions are thus robust with respect to the somewhat arbitrary choice
 344 of the hydrodynamic roughnesses in the use of the data from ERA5-Land
 345 reanalysis.

346 4 Discussion and conclusion

347 The feedback of the giant dunes on the wind flow has important implications
 348 for smaller scales bedforms. As illustrated in Fig. 9, small linear dunes (~ 50 m
 349 wide) are often present in the 1–2 km interdune between giant linear dunes in
 350 the Namib Sand Sea (Livingstone et al. 2010). These smaller dunes do not ex-
 351 hibit the same orientation as the large ones, and are sometimes named ‘crossing
 352 dunes’ (Chandler et al. 2022). Whilst differences between large and small scale
 353 dune patterns are observed ubiquitously, they are largely usually attributed
 354 to the presence of two different dune growth mechanisms, leading to two dif-
 355 ferent dune patterns (orientations and/or morphologies) for the same wind
 356 regime (Courrech du Pont et al. 2014; Runyon et al. 2017; Lü et al. 2017; Song
 357 et al. 2019; Gadal et al. 2020; Hu et al. 2021). Here, however, our arguments
 358 enable the development of differing orientations for the small and giant lin-
 359 ear dunes whilst also imposing governed by the same dune growth mechanism
 360 (elongating mode). Figure 9 shows how the orientations for the small and giant
 361 dunes can be derived from the locally measured and regionally predicted winds
 362 respectively (red arrows in Fig. 9). These predictions require a specification
 363 for to specify the threshold of eolian aeolian sand transport. Importantly, its
 364 value expressed as (a shear velocity $u_{th} \approx 0.15 \text{ ms}^{-1}$ is reached in the deflected
 365 wind regime already estimated at $u_{th} \approx 0.15 \text{ m s}^{-1}$) can be reached in periods
 366 during which winds are deflected (recall that the stronger winds, responsible
 367 for most of the sediment transport and associated dune morphodynamics, are
 368 not deflected – see Fig. 6). The feedback of the giant dunes on the wind de-
 369 scribed in this study through wind deflection and attenuation, thus provides
 370 a potential explanation for the existence of these small linear dunes elongating
 371 across the interdune, a dynamic which has remained unresolved to date. These
 372 crossing dunes could provide additional constraints for the inference of local
 373 winds from bedforms, similarly to that currently performed on Mars using rip-
 374 ple orientations (Liu and Zimbelman 2015; Hood et al. 2021). Further work is
 375 needed to investigate these processes in more detail, including measurements
 376 of sediment transport and flow on the top of dunes.

377 This study presents the evidence that wind flow patterns around giant
 378 dunes are influenced by the atmospheric boundary layer, particularly during
 379 nocturnal conditions. It leaves However, we do not address here the question
 380 of the limitation of their pattern coarsening, and leave open the debate as
 381 to whether the size of giant dunes is limited controlled by the depth of this
 382 layer (Andreotti et al. 2009), in contrast to an unconstrained dune growth,
 383 sediment supply limited and ever-slower with size (Gunn et al. 2021a) growth
 384 with size (Werner and Kocurek 1999; Gunn et al. 2021a). More field evidence
 385 is definitively needed from additional dune fields, but this mechanism would
 386 then allow for the inference of the ABL depth from giant bedform wavelengths
 387 where measurements are not feasible or available, such as Titan (Lorenz et al.
 388 2010).

389 To conclude on conditions under which the ERA5-Land reanalysis data can
 390 reliably be used to study dune morphodynamics, we summarise the compari-

son of local (direct measurements) and regional (climate reanalysis) wind data as follows. In flat areas, the agreement between the two confirms the ability of the ERA5-Land climate reanalysis to predict the wind regime down to scales ~ 10 km, i.e the model grid. When smaller scale topographies are present (giant dunes in our case), locally measured winds can significantly differ from the regionally predicted ones. This is the case when the disturbances induced by the dunes interact with the lower part of the ABL vertical structure, which presents circadian variations. During the day, when the capping layer is typically high, this interaction is small, and the ERA5-Land predictions are also quantitatively consistent with the local data. During the night, however, the presence of a shallow atmospheric boundary layer induces a strong confinement of the flow, and is associated with large wind deflection by the dunes. Importantly, we find that this effect can be counterbalanced for large wind velocities, which are capable of deforming the capping layer, thus decreasing the influence of the confinement.

The theoretical computation of the wind disturbances induced by sinusoidal ridges under flow confinement has been performed in the linear limit (Andreotti et al. 2009, 2012), i.e. when the aspect ~~ration~~-ratio of these ridges is small ($k\xi_0 \ll 1$). These models are able to qualitatively reproduce the observed wind deflection (Appendix 1, Online Resource Figs. S11 and S13), and thus provide the physical support for the interpretation we propose here based on hydrodynamic regimes. However, these models cannot quantitatively predict the magnitude of ~~these~~-our observations, probably due to the presence of expected non-linearities in high confinement situations linked to strong flow modulations. Besides, these linear calculations only predict wind attenuation in the interdune, in contrast with the observed enhanced velocities associated with particular evening winds from the South during the period October–March (Online Resource Fig. S12). Some other models predict different spatial flow structures in response to a modulated topography, such as lee waves and rotors (Baines 1995; Vosper 2004). However, our measurements are located at a single point in the interdune, ~~so we are and we are thus~~ unable to explore these types of responses. Data at different places along and across the ridges are needed to investigate and possibly map such flow structures, and for further comparisons with the models.

Acknowledgements We would like to acknowledge the contributors of the following open-source python libraries, Matplotlib (Hunter 2007), Numpy (Harris et al. 2020) and Scipy (Virtanen et al. 2020), which provide an incredibly efficient ecosystem allowing scientific research in Python. We also thank B. Andreotti and A. Gunn for useful discussions.

All data used in this study can be found in Gadal et al. (2022). Note that it contains modified Copernicus Climate Change Service Information (2021). Neither the European Commission nor ECMWF is responsible for any use that may be made of the Copernicus Information or Data it contains. Fully documented codes used Documented codes used in this study to analyse this study data are available at <https://github.com/Cgadal/GiantDunes> (will be made public upon acceptance of this manuscript for publication).

Multiple grants have supported the collection of wind data through visits to the four sites between 2013 and 2020 (John Fell Oxford University Press (OUP) Research Fund (121/474); National Geographic (CP-029R-17); Natural Environment Research Council UK

(NE/R010196/1 and NE/H021841/1 NSFGEO-NERC); Southampton Marine and Maritime Institute SMMI EPSRC-GCRF UK), along with research permits (1978/2014, 2140/2016, 2304/2017, 2308/2017, RPIV00022018, RPIV0052018, RPIV00230218). The authors are very grateful for support from Etosha National Park (especially Shyane Kötting, Boas Erckie, Pierre du Preez, Claudine Cloete, Immanuel Kapofi, Wilferd Versfeld, and Werner Kilian), Gobabeb Namib Research Institute (Gillian Maggs-Kölling and Eugene Marais), The Skeleton Coast National Park (Joshua Kazeurua). Various researchers and desert enthusiasts have assisted with instruments and the logistics of expeditions, especially Mary Seely for expert guidance at the North Sand Sea site.

Finally, we acknowledge financial support from the Laboratoire d'Excellence UnivEarthS Grant ANR-10-LABX-0023, the Initiative d'Excellence Université de Paris Grant ANR-18-IDEX-0001, the French National Research Agency Grants ANR-17-CE01-0014/SONO and the National Science Center of Poland Grant 2016/23/B/ST10/01700.

Appendix 1: Linear theory of wind response to topographic perturbation

Following the work of Fourrière et al. (2010), Andreotti et al. (2012) and Andreotti et al. (2009), we briefly describe in this appendix the framework for the linear response of a turbulent flow to a topographic perturbation of small aspect ratio. As a general bed elevation can be decomposed into Fourier modes, we focus here on a sinusoidal topography:

$$\xi = \xi_0 \cos [k (\cos(\alpha)y - \sin(\alpha)x)], \quad (3)$$

which is also a good approximation for the giant dunes observed in the North Sand Sea and South Sand Sea Station (Fig. 2 and Online Resource Fig. S4). Here, x and y are the streamwise and spanwise coordinates, $k = 2\pi/\lambda$ the wavenumber of the sinusoidal perturbation, α its crest orientation with respect to the x -direction (anticlockwise) and ξ_0 its amplitude. The two components of the basal shear stress $\tau = \rho_0 u_* \mathbf{u}_*$, constant in the flat bottom reference case, can then be generically written as:

$$\tau_x = \tau_0 \left(1 + k \xi_0 \sqrt{\mathcal{A}_x^2 + \mathcal{B}_x^2} \cos [k (\cos(\alpha)y - \sin(\alpha)x) + \phi_x] \right), \quad (4)$$

$$\tau_y = \tau_0 k \xi_0 \sqrt{\mathcal{A}_y^2 + \mathcal{B}_y^2} \cos [k (\cos(\alpha)y - \sin(\alpha)x) + \phi_y], \quad (5)$$

where τ_0 is the reference basal shear stress on a flat bed. We have defined the phase $\phi_{x,y} = \tan^{-1}(\mathcal{B}_{x,y}/\mathcal{A}_{x,y})$ from the in-phase and in-quadrature hydrodynamical coefficients $\mathcal{A}_{x,y}$ and $\mathcal{B}_{x,y}$. They are functions of k and of the flow conditions, i.e the bottom roughness, the vertical flow structure and the incident flow direction, and the theoretical framework developed in the above cited papers proposes methods to compute them in the linear regime.

⁴⁷¹ Following Andreotti et al. (2012), the effect of the incident wind direction
⁴⁷² can be approximated by the following expressions:

$$\mathcal{A}_x = \mathcal{A}_0 \sin^2 \alpha, \quad (6)$$

$$\mathcal{B}_x = \mathcal{B}_0 \sin^2 \alpha, \quad (7)$$

$$\mathcal{A}_y = -\frac{1}{2} \mathcal{A}_0 \cos \alpha \sin \alpha, \quad (8)$$

$$\mathcal{B}_y = -\frac{1}{2} \mathcal{B}_0 \cos \alpha \sin \alpha, \quad (9)$$

⁴⁷³ where \mathcal{A}_0 and \mathcal{B}_0 are now two coefficients independent of the dune orientation
⁴⁷⁴ α , corresponding to the transverse case ($\alpha = 90^\circ$). ~~For~~^{In the case of} a fully
⁴⁷⁵ turbulent boundary layer capped by a stratified atmosphere, these coefficients
⁴⁷⁶ depend on kH , kz_0 , \mathcal{F} and \mathcal{F}_I (Andreotti et al. 2009). ~~In this study~~^{For their}
⁴⁷⁷ ~~computation~~, we assume ~~here~~ a constant hydrodynamic roughness $z_0 \simeq 1$ mm
⁴⁷⁸ (Online Resource section 1). For the considered giant dunes, this leads to
⁴⁷⁹ $kz_0 \simeq 2 \cdot 10^{-6}$, as their wavelength is $\lambda \simeq 2.4$ km (or $k \simeq 2 \cdot 10^{-3} \text{ m}^{-1}$). Values
⁴⁸⁰ of z_0 extracted from field data indeed typically fall between 0.1 mm and 10
⁴⁸¹ mm (Sherman and Farrell 2008; Field and Pelletier 2018). Importantly, \mathcal{A}_0
⁴⁸² and \mathcal{B}_0 do not vary much in the corresponding range of kz_0 (Fourrière et al.
⁴⁸³ 2010), and the results presented here are robust with respect to this choice.

⁴⁸⁴ With capping layer height and Froude numbers computed from the ERA5-
⁴⁸⁵ Land time series, the corresponding \mathcal{A}_0 and \mathcal{B}_0 can be deduced, as displayed
⁴⁸⁶ in Online Resource Fig. S13. Interestingly, it shows similar regimes as in the
⁴⁸⁷ diagrams of Fig. 8 and Online Resource Fig. S11a,b, supporting the underlying
⁴⁸⁸ physics. However, the agreement is qualitative only. Further, the linearity
⁴⁸⁹ assumption of the theoretical framework requires $(|\tau| - \tau_0)/\tau_0 \ll 1$, which
⁴⁹⁰ translates into $k\xi\sqrt{\mathcal{A}_0^2 + \mathcal{B}_0^2} \ll 1$. In our case, the giant dune morphology
⁴⁹¹ gives $k\xi_0 \simeq 0.1$, which means that one quits the regime of validity of the
⁴⁹² linear theory when the coefficient modulus $\sqrt{\mathcal{A}_0^2 + \mathcal{B}_0^2}$ becomes larger than a
⁴⁹³ few units. In accordance with the theoretical expectations, these coefficients
⁴⁹⁴ present values on the order of unity ($\mathcal{A}_0 \simeq 3$ and $\mathcal{B}_0 \simeq 1$) in unconfined sit-
⁴⁹⁵ uations (Claudin et al. 2013; Lü et al. 2021). In contrast and as illustrated
⁴⁹⁶ in Online Resource Fig. S13a,b, larger values are predicted in case of strong
⁴⁹⁷ confinement, which does not allow us to proceed to further quantitative com-
⁴⁹⁸ parison with the data.

⁴⁹⁹ Finally, the linear model is also able to reproduce the enhancement of the
⁵⁰⁰ flow deflection over the sinusoidal ridges when $\sqrt{\mathcal{A}_0^2 + \mathcal{B}_0^2}$ is increased (Online
⁵⁰¹ Resource Fig. S13). Here, using $k\xi_0 \simeq 0.1$ to be representative of the amplitude
⁵⁰² of the giant dunes at the North Sand Sea station, the coefficient modulus is
⁵⁰³ bounded to 10.

504 **Appendix 2: Sediment transport and dune morphodynamics**

505 We summarise in this appendix the sediment transport and dune morphodynamics
 506 theoretical framework leading to the prediction of sand fluxes and dune
 507 orientations from wind data.

508 *Sediment transport* — The prediction of sand fluxes from wind data has been
 509 a long standing issue in aeolian geomorphological studies (Fryberger and Dean
 510 1979; Pearce and Walker 2005; Sherman and Li 2012; Shen et al. 2019). Based
 511 on laboratory studies in wind tunnels (Rasmussen et al. 1996; Iversen and
 512 Rasmussen 1999; Creyssels et al. 2009; Ho et al. 2011), as well as physical
 513 considerations (Ungar and Haff 1987; Andreotti 2004; Durán et al. 2011; Pähzt
 514 and Durán 2020), it has been shown that the steady saturated saltation flux
 515 over a flat sand bed depends linearly on the shear stress:

$$\frac{q_{\text{sat}}}{Q} = \Omega \sqrt{\Theta_{\text{th}}} (\Theta - \Theta_{\text{th}}), \quad (10)$$

516 where Ω is a proportionality constant, $Q = d\sqrt{(\rho_s - \rho_0)gd/\rho_0}$ is a character-
 517 istic flux, $\Theta = \rho_0 u_*^2 / (\rho_s - \rho_0)gd$ the Shields number, and Θ_{th} its threshold
 518 value below which saltation vanishes. $\rho_s = 2.6 \text{ g cm}^{-3}$ and $d = 180 \mu\text{m}$ are
 519 the grain density and diameter, and g is the gravitational acceleration. The
 520 shear velocity, and consequently the Shields number as well as the sediment
 521 flux, are time dependent.

522 Recently, Pähzt and Durán (2020) suggested an additional quadratic term
 523 in Shields to account for grain-grain interactions within the transport layer at
 524 strong wind velocities:

$$\frac{q_{\text{sat}, t}}{Q} = \frac{2\sqrt{\Theta_{\text{th}}}}{\kappa\mu} (\Theta - \Theta_{\text{th}}) \left(1 + \frac{C_M}{\mu} [\Theta - \Theta_{\text{th}}] \right), \quad (11)$$

525 where $\kappa = 0.4$ is the von Kármán constant, $C_M \simeq 1.7$ a constant and $\mu \simeq 0.6$ is
 526 a friction coefficient, taken to be the avalanche slope of the granular material.
 527 The fit of this law to the experimental data of Creyssels et al. (2009) and Ho
 528 et al. (2011) gives $\Theta_{\text{th}} = 0.0035$. The fit of Eq. 10 on these same data similarly
 529 gives $\Omega \simeq 8$ and $\Theta_{\text{th}} = 0.005$. The sand flux angular distributions and the
 530 dune orientations in Fig. 9 are calculated using this law (11). We have checked
 531 that using the ordinary linear relationship (10) instead does not change the
 532 predicted dune orientations by more than a few degrees.

533 *Dune orientations* — Dune orientations are predicted with the dimensional
 534 model of Courrech du Pont et al. (2014), from the sand flux time series com-
 535 puted with the above transport law. Two orientations are possible depending
 536 on the mechanism dominating the dune growth: elongation or bed instabil-
 537 ity. The orientation α corresponding the bed instability is then the one that
 538 maximises the following growth rate (Rubin and Hunter 1987):

$$\sigma \propto \frac{1}{H_d W_d T} \int_0^T q_{\text{crest}} |\sin(\theta - \alpha)| dt, \quad (12)$$

539 where θ is the wind orientation measured with respect to the same reference
 540 as α , and H_d and W_d are dimensional constants respectively representing the
 541 dune height and width. The integral runs over a time T , which must be repre-
 542 sentative of the characteristic period of the wind regime. The flux at the crest
 543 is expressed as:

$$q_{\text{crest}} = q_{\text{sat}} [1 + \gamma |\sin(\theta - \alpha)|], \quad (13)$$

544 where the flux-up ratio γ has been calibrated to 1.6 using field studies, under-
 545 water laboratory experiments and numerical simulations. Predictions of the
 546 linear analysis of Gadal et al. (2019) and Delorme et al. (2020) give similar
 547 results.

548 Similarly, the dune orientation corresponding to the elongation mechanism
 549 is the one that verifies:

$$\tan(\alpha) = \frac{\langle q_{\text{crest}}(\alpha) \mathbf{e}_\theta \rangle \cdot \mathbf{e}_{WE}}{\langle q_{\text{crest}}(\alpha) \mathbf{e}_\theta \rangle \cdot \mathbf{e}_{SN}}, \quad (14)$$

550 where $\langle \cdot \rangle$ denotes a vectorial time average. The unitary vectors \mathbf{e}_{WE} , \mathbf{e}_{SN} and
 551 \mathbf{e}_θ are in the West-East, South-North and wind directions, respectively.

552 The resulting computed dune orientations, blue and red arrows in Fig. 9,
 553 then depend on a certain number of parameters (grain properties, flux-up ratio,
 554 etc.), for which we take typical values for aeolian sandy deserts. Due to the lack
 555 of measurements in the studied places, some uncertainties can be expected. We
 556 therefore run a sensitivity test by calculating the dune orientations for grain
 557 diameters ranging from 100 μm to 400 μm and for a speed-up ratio between
 558 0.1 and 10 (wedges in Fig. 9).

559 References

- 560 Andreotti B (2004) A two-species model of aeolian sand transport. *J Fluid
Mech* 510:47–70
- 562 Andreotti B, Claudin P, Douady S (2002) Selection of dune shapes and veloc-
563 ities part 1: Dynamics of sand, wind and barchans. *The European Physical
564 Journal B-Condensed Matter and Complex Systems* 28:321–339
- 565 Andreotti B, Fourrière A, Ould-Kaddour F, Murray B, Claudin P (2009) Gi-
566 ant aeolian dune size determined by the average depth of the atmospheric
567 boundary layer. *Nature* 457:1120–1123
- 568 Andreotti B, Claudin P, Devauchelle O, Durán O, Fourrière A (2012) Bedforms
569 in a turbulent stream: ripples, chevrons and antidunes. *J Fluid Mech* 690:94–
570 128
- 571 Ashkenazy Y, Yizhaq H, Tsoar H (2012) Sand dune mobility under climate
572 change in the kalahari and australian deserts. *Climatic Change* 112:901–923
- 573 Baddock M, Livingstone I, Wiggs G (2007) The geomorphological significance
574 of airflow patterns in transverse dune interdunes. *Geomorphology* 87:322–
575 336
- 576 Bagnold RA (1941) *The Physics of Blown Sand and Desert Dunes*. London :
577 Methuen : Chapman & Hall
- 578 Baines PG (1995) Topographic effects in stratified flows. Cambridge university
579 press
- 580 Bauer BO, Sherman DJ, Wolcott JF (1992) Sources of uncertainty in shear
581 stress and roughness length estimates derived from velocity profiles. *The
582 Professional Geographer* 44:453–464
- 583 Belcher S, JCR H (1998) Turbulent flow over hills and waves. *Annu Rev Fluid
584 Mech* 30:507–538
- 585 Blumberg DG, Greeley R (1996) A comparison of general circulation model
586 predictions to sand drift and dune orientations. *J Clim* 9:3248–3259
- 587 Bristow NR, Best J, Wiggs GFS, Nield JM, Baddock MC, Delorme P, Chris-
588 tensen KT (2022) Topographic perturbation of turbulent boundary layers
589 by low-angle, early-stage aeolian dunes. *Earth Surf Process Landf* n/a, DOI
590 <https://doi.org/10.1002/esp.5326>
- 591 Brookfield M (1977) The origin of bounding surfaces in ancient aeolian sand-
592 stones. *Sedimentology* 24:303–332
- 593 Brown S, Nickling WG, Gillies JA (2008) A wind tunnel examination of shear
594 stress partitioning for an assortment of surface roughness distributions. *J
595 Geophys Res* 113:F02S06
- 596 Chandler C, Radebaugh J, McBride J, Morris T, Narteau C, Arnold K, Lorenz
597 R, Barnes J, Hayes A, Rodriguez S, Rittenour T (2022) Near-surface struc-
598 ture of a large linear dune and an associated crossing dune of the northern
599 namib sand sea from ground penetrating radar: Implications for the his-
600 tory of large linear dunes on earth and titan. *Aeolian Research* 57:100813,
601 DOI <https://doi.org/10.1016/j.aeolia.2022.100813>
- 602 Chang H, Simons D (1970) The bed configuration of straight sand-bed channels
603 when flow is nearly critical. *J Fluid Mech* 42:491–495

- 604 Charru F, Andreotti B, Claudin P (2013) Sand ripples and dunes. *Annu Rev
605 Fluid Mech* 45:469–493
- 606 Claudin P, Wiggs G, Andreotti B (2013) Field evidence for the upwind velocity
607 shift at the crest of low dunes. *Boundary-Layer Meteorol* 148:195–206
- 608 Claudin P, Durán O, Andreotti B (2017) Dissolution instability and roughen-
609 ing transition. *J Fluid Mech* 832:R2
- 610 Claudin P, Louge M, Andreotti B (2021) Basal pressure variations induced by
611 a turbulent flow over a wavy surface. *Frontiers in Physics* 9:682564
- 612 Colombini M (2004) Revisiting the linear theory of sand dune formation. *J
613 Fluid Mech* 502:1–16
- 614 Courrech du Pont S (2015) Dune morphodynamics. *C R Phys* 16:118–138
- 615 Courrech du Pont S, Narteau C, Gao X (2014) Two modes for dune orientation.
616 *Geology* 42:743–746
- 617 Creyssels M, Dupont P, El Moctar AO, Valance A, Cantat I, Jenkins JT, Pasini
618 JM, Rasmussen KR (2009) Saltating particles in a turbulent boundary layer:
619 experiment and theory. *J Fluid Mech* 625:47–74
- 620 de Winter W, Donker J, Sterk G, Van Beem J, Ruessink G (2020) Regional
621 versus local wind speed and direction at a narrow beach with a high and
622 steep foredune. *Plos one* 15:e0226983
- 623 Dee DP, Uppala SM, Simmons AJ, Berrisford P, Poli P, Kobayashi S, Andrae
624 U, Balmaseda M, Balsamo G, Bauer dP, et al. (2011) The era-interim re-
625 analysis: Configuration and performance of the data assimilation system. *Q
626 J R Meteorol Soc* 137:553–597
- 627 Delorme P, Wiggs G, Baddock M, Claudin P, Nield J, Valdez A (2020) Dune
628 initiation in a bimodal wind regime. *J Geophys Res* 125:e2020JF005757
- 629 Durán O, Claudin P, Andreotti B (2011) On aeolian transport: Grain-scale
630 interactions, dynamical mechanisms and scaling laws. *Aeolian Res* 3:243–
631 270
- 632 Durran DR (1990) Mountain waves and downslope winds. In: *Atmospheric
633 processes over complex terrain*, Springer, pp 59–81
- 634 Dyer A (1974) A review of flux-profile relationships. *Boundary-Layer Meteorol
635* 7:363–372
- 636 Ewing RC, Kocurek G, Lake LW (2006) Pattern analysis of dune-field param-
637 eters. *Earth Surf Process Landf* 31:1176–1191
- 638 Farr TG, Rosen PA, Caro E, Crippen R, Duren R, Hensley S, Kobrick M,
639 Paller M, Rodriguez E, Roth L, et al. (2007) The shuttle radar topography
640 mission. *Rev Geophys* 45
- 641 Fernando H, Mann J, Palma J, Lundquist JK, Barthelmie RJ, Belo-Pereira M,
642 Brown W, Chow F, Gerz T, Hocut C, et al. (2019) The perdigão: Peering
643 into microscale details of mountain winds. *Bull Am Meteorol Soc* 100:799–
644 819
- 645 Field JP, Pelletier JD (2018) Controls on the aerodynamic roughness length
646 and the grain-size dependence of aeolian sediment transport. *Earth Surf
647 Process Landf* 43:2616–2626
- 648 Finnigan J, Raupach M, Bradley E, Aldis G (1990) A wind tunnel study
649 of turbulent flow over a two-dimensional ridge. *Boundary-Layer Meteorol*

- 650 50:277–317
- 651 Finnigan J, Ayotte K, Harman I, Katul G, Oldroyd H, Patton E, Poggi D,
652 Ross A, Taylor P (2020) Boundary-layer flow over complex topography.
Boundary-Layer Meteorol 177:247–313
- 653 Flack K, Schultz M (2010) Review of hydraulic roughness scales in the fully
654 rough regime. Journal of Fluids Engineering 132:041203
- 655 Fourrière A, Claudin P, Andreotti B (2010) Bedforms in a turbulent stream:
656 formation of ripples by primary linear instability and of dunes by nonlinear
657 pattern coarsening. J Fluid Mech 649:287–328
- 658 Frederick KA, Hanratty TJ (1988) Velocity measurements for a turbulent non-
659 separated flow over solid waves. Exp Fluids 6:477–486
- 660 Fryberger SG, Dean G (1979) Dune forms and wind regime. A study of global
661 sand seas 1052:137–169
- 662 Gadal C, Narteau C, Courrech Du Pont S, Rozier O, Claudin P (2019) Incip-
663 ent bedforms in a bidirectional wind regime. J Fluid Mech 862:490–516
- 664 Gadal C, Narteau C, Courrech du Pont S, Rozier O, Claudin P (2020) Peri-
665 odicity in fields of elongating dunes. Geology 48:343–347
- 666 Gadal C, Delorme P, Narteau C, Wiggs G, Baddock M, Nield JM, Claudin
667 P (2022) Data used in 'Local wind regime induced by giant linear dunes:
668 comparison of ERA5-Land re-analysis with surface measurements'. DOI
669 10.5281/zenodo.6343138
- 670 Garratt JR (1994) The atmospheric boundary layer. Earth-Science Reviews
671 37:89–134
- 672 Garvey B, Castro IP, Wiggs G, Bullard J (2005) Measurements of flows over
673 isolated valleys. Boundary-Layer Meteorol 117:417–446
- 674 Gong W, Ibbetson A (1989) A wind tunnel study of turbulent flow over model
675 hills. Boundary-Layer Meteorol 49:113–148
- 676 Gong W, Taylor P, Dörnbrack A (1996) Turbulent boundary-layer flow over
677 fixed aerodynamically rough two-dimensional sinusoidal waves. J Fluid Mech
678 312:1–37
- 679 Guérin A, Derr J, Du Pont SC, Berhanu M (2020) Streamwise dissolution
680 patterns created by a flowing water film. Phys Rev Lett 125:194502
- 681 Gunn A, Casasanta G, Di Liberto L, Falcini F, Lancaster N,
682 Jerolmack DJ (2021a) What sets aeolian dune height? DOI
683 <https://doi.org/10.31223/X5QG8S>
- 684 Gunn A, Wanker M, Lancaster N, Edmonds D, Ewing R, Jerolmack
685 D (2021b) Circadian rhythm of dune-field activity. Geophys Res Lett
686 48:e2020GL090924
- 687 Harris CR, Millman KJ, van der Walt SJ, Gommers R, Virtanen P, Cournau-
688 peau D, Wieser E, Taylor J, Berg S, Smith NJ, et al. (2020) Array program-
689 ming with numpy. Nature 585:357–362
- 690 Havholm KG, Kocurek G (1988) A preliminary study of the dynamics of a
691 modern draa, algodones, southeastern california, usa. Sedimentology 35:649–
692 669
- 693 Hersbach H, Bell B, Berrisford P, Hirahara S, Horányi A, Muñoz-Sabater J,
694 Nicolas J, Peubey C, Radu R, Schepers D, et al. (2020) The era5 global

- 696 reanalysis. *Q J R Meteorol Soc* 146:1999–2049
- 697 Hesp P, Illenberger W, Rust I, McLachlan A, Hyde R (1989) Some aspects of
698 transgressive dunefield and transverse dune geomorphology and dynamics,
699 south coast, south africa. *Zeitschrift fur Geomorphologie*, Supplementband
700 73:111–123
- 701 Hesp PA, Hastings K (1998) Width, height and slope relationships and aero-
702 dynamic maintenance of barchans. *Geomorphology* 22:193–204
- 703 Hesp PA, Smyth TAG, Nielsen P, Walker IJ, Bauer BO, Davidson-Arnott R
704 (2015) Flow deflection over a foredune. *Geomorphology* 230:64–74
- 705 Ho TD, Valance A, Dupont P, Ould El Moctar A, Tuan Duc H, Valance A,
706 Dupont P, Ould El Moctar A (2011) Scaling laws in aeolian sand transport.
707 *Phys Rev Lett* 106:4–7
- 708 Hood DR, Ewing RC, Roback KP, Runyon K, Avouac JP, McEnroe M (2021)
709 Inferring airflow across martian dunes from ripple patterns and dynamics.
710 *Frontiers in Earth Science* 9:702828
- 711 Howard AD (1977) Effect of slope on the threshold of motion and its applica-
712 tion to orientation of wind ripples. *Geological Society of America Bulletin*
713 88:853–856
- 714 Hu Z, Gao X, Lei J, Zhou N (2021) Geomorphology of aeolian dunes in the
715 western sahara desert. *Geomorphology* 392:107916
- 716 Hunt J, Leibovich S, Richards K (1988) Turbulent shear flows over low hills.
717 *Q J R Meteorol Soc* 114:1435–1470
- 718 Hunt JCR, Vilenski GG, Johnson ER (2006) Stratified separated flow around
719 a mountain with an inversion layer below the mountain top. *J Fluid Mech*
720 556:105–119
- 721 Hunter JD (2007) Matplotlib: A 2d graphics environment. *Computing in sci-
722 ence & engineering* 9:90–95
- 723 Hunter RE, Richmond BM, Alpha TR (1983) Storm-controlled oblique dunes
724 of the oregon coast. *Geol Soc America Bull* 94:1450–1465
- 725 Iversen JD, Rasmussen KR (1999) The effect of wind speed and bed slope on
726 sand transport. *Sedimentology* 46:723–731
- 727 Jackson PS, Hunt JCR (1975) Turbulent wind flow over a low hill. *Q J R
728 Meteorol Soc* 101:929–955
- 729 Jiang Q (2014) Applicability of reduced-gravity shallow-water theory to atmo-
730 spheric flow over topography. *J Atmos Sci* 71:1460–1479
- 731 Jolivet M, Braucher R, Dovchintseren D, Hocquet S, Schmitt J, ASTER Team
732 (2021) Erosion around a large-scale topographic high in a semi-arid sedimen-
733 tary basin: Interactions between fluvial erosion, aeolian erosion and aeolian
734 transport. *Geomorphology* 386:107747
- 735 Kennedy JF (1963) The mechanics of dunes and antidunes in erodible-bed
736 channels. *J Fluid Mech* 16:521–544
- 737 Kim HG, Patel VC, Lee CM (2000) Numerical simulation of wind flow over
738 hilly terrain. *J Wind Eng Ind Aerodyn* 87:45–60
- 739 Kroy K, Sauermann G, Herrmann HJ (2002) Minimal model for aeolian sand
740 dunes. *Phys Rev E* 66:031302

- 741 Lancaster J, Lancaster N, Seely M (1984) Climate of the central namib desert.
742 Madoqua 1984:5–61
- 743 Lancaster N (1985) Winds and sand movements in the namib sand sea. Earth
744 Surf Process Landf 10:607–619
- 745 Lancaster N, Nickling W, Neuman CM, Wyatt V (1996) Sediment flux and
746 airflow on the stoss slope of a barchan dune. Geomorphology 17:55–62
- 747 Lewis HW, Mobbs SD, Lehning M (2008) Observations of cross-ridge flows
748 across steep terrain. Q J R Meteorol Soc 134:801–816
- 749 Liu ZYC, Zimbelman JR (2015) Recent near-surface wind directions inferred
750 from mapping sand ripples on martian dunes. Icarus 261:169–181
- 751 Livingstone I, Warren A (2019) Aeolian geomorphology: a new introduction.
752 Wiley
- 753 Livingstone I, Bristow C, Bryant RG, Bullard J, White K, Wiggs GFS, Baas
754 ACW, Bateman MD, Thomas DSG (2010) The namib sand sea digital
755 database of aeolian dunes and key forcing variables. Aeolian Res 2:93–104
- 756 Lorenz R, Claudin P, Andreotti B, Radebaugh J, Tokano T (2010) A 3 km
757 atmospheric boundary layer on titan indicated by dune spacing and huygens
758 data. Icarus 205:719–721
- 759 Lü P, Narteau C, Dong Z, Rozier O, Du Pont SC (2017) Unravelling raked
760 linear dunes to explain the coexistence of bedforms in complex dunefields.
761 Nature communications 8:1–9
- 762 Lü P, Narteau C, Dong Z, Claudin P, Rodriguez S, An Z, Fernandez-Cascales
763 L, Gadal C, Courrech du Pont S (2021) Direct validation of dune instability
764 theory. Proceedings of the National Academy of Sciences 118
- 765 Mason P, Sykes R (1979) Flow over an isolated hill of moderate slope. Q J R
766 Meteorol Soc 105:383–395
- 767 McKenna Neuman C, Lancaster N, Nickling WG (1997) Relations between
768 dune morphology, air flow, and sediment flux on reversing dunes, Silver Peak,
769 Nevada. Sedimentology 44:1103–1111, DOI 10.1046/j.1365-3091.1997.d01-
770 61.x
- 771 Mizumura K (1995) Free-surface profile of open-channel flow with wavy bound-
772 ary. J Hydraul Eng 121:533–539
- 773 Monin AS, Obukhov AM (1954) Basic laws of turbulent mixing in the surface
774 layer of the atmosphere. Contrib Geophys Inst Acad Sci USSR 151:e187
- 775 Mulligan KR (1988) Velocity profiles measured on the windward slope of a
776 transverse dune. Earth Surf Process Landf 13:573–582
- 777 Muñoz-Sabater J, Dutra E, Agustí-Panareda A, Albergel C, Arduini G, Bal-
778 samo G, Boussetta S, Choulga M, Harrigan S, Hersbach H, et al. (2021)
779 Era5-land: A state-of-the-art global reanalysis dataset for land applications.
780 Earth Syst Sci Data 13:4349–4383
- 781 Nield JM, King J, Wiggs GFS, Leyland J, Bryant RG, Chiverrell RC, Darby
782 SE, Eckhardt FD, Thomas DSG, Vircavs LH, Washington R (2014) Esti-
783 mating aerodynamic roughness over complex surface terrain. J Geophys Res
784 118:12948–12961
- 785 Nield JM, Wiggs GF, Baddock MC, Hipondoka MH (2017) Coupling leeside
786 rainfall to avalanche characteristics in aeolian dune dynamics. Geology

- 787 45:271–274
- 788 Pähzt T, Durán O (2020) Unification of aeolian and fluvial sediment transport
789 rate from granular physics. *Phys Rev Lett* 124:168001
- 790 Pearce KI, Walker IJ (2005) Frequency and magnitude biases in the 'Fryberger'
791 model, with implications for characterizing geomorphically effective winds.
792 *Geomorphology* 68:39–55
- 793 Pelletier JD, Field JP (2016) Predicting the roughness length of turbulent flows
794 over landscapes with multi-scale microtopography. *Earth Surface Dynamics*
795 4:391–405
- 796 Poggi D, Katul G, Albertson J, Ridolfi L (2007) An experimental investigation
797 of turbulent flows over a hilly surface. *Phys Fluids* 19:036601
- 798 Rasmussen KR (1989) Some aspects of flow over coastal dunes. *Proceedings of*
799 *the Royal Society of Edinburgh, Section B: Biological Sciences* 96:129–147
- 800 Rasmussen KR, Iversen JD, Rautaheimo P (1996) Saltation and wind flow
801 interaction in a variable slope wind tunnel. *Geomorphology* 17:19–28
- 802 Raupach M (1992) Drag and drag partition on rough surfaces. *Boundary-Layer*
803 *Meteorol* 60:375–395
- 804 Rubin DM, Hunter RE (1987) Bedform alignment in directionally varying
805 flows. *Science* 237:276–278
- 806 Runyon K, Bridges N, Ayoub F, Newman C, Quade J (2017) An integrated
807 model for dune morphology and sand fluxes on mars. *Earth and Planetary*
808 *Science Letters* 457:204–212
- 809 Sauermann G, Andrade Jr J, Maia L, Costa U, Araújo A, Herrmann H
810 (2003) Wind velocity and sand transport on a barchan dune. *Geomorphol-*
811 *ogy* 54:245–255
- 812 Seidel DJ, Zhang Y, Beljaars A, Golaz JC, Jacobson AR, Medeiros B (2012)
813 Climatology of the planetary boundary layer over the continental united
814 states and europe. *J Geophys Res* 117:D17106
- 815 Shao Y (2008) Physics and modelling of wind erosion, vol 37. Springer Science
816 & Business Media
- 817 Shen Y, Zhang C, Huang X, Wang X, Cen S (2019) The effect of wind speed
818 averaging time on sand transport estimates. *Catena* 175:286–293
- 819 Sheridan PF, Vosper SB (2006) A flow regime diagram for forecasting lee
820 waves, rotors and downslope winds. *Meteorol Appl* 13:179–195
- 821 Sherman CA (1978) A mass-consistent model for wind fields over complex
822 terrain. *J Appl Meteorol Clim* 17:312–319
- 823 Sherman D, Farrell E (2008) Aerodynamic roughness lengths over movable
824 beds: Comparison of wind tunnel and field data. *J Geophys Res* 113:1–10
- 825 Sherman DJ, Li B (2012) Predicting aeolian sand transport rates: A reevalu-
826 ation of models. *Aeolian Res* 3:371–378
- 827 Smith AB, Jackson DWT, Cooper JAG (2017) Three-dimensional airflow and
828 sediment transport patterns over barchan dunes. *Geomorphology* 278:28–42
- 829 Song Q, Gao X, Lei J, Li S (2019) Spatial distribution of sand dunes and their
830 relationship with fluvial systems on the southern margin of the taklimakan
831 desert, china. *Geomatics, Natural Hazards and Risk* 10:2408–2428

- 832 Spalding DB (1961) A single formula for the law of the wall. *Journal of Applied*
833 *Mechanics* 28:455–458
- 834 Stull R (2006) 9 - the atmospheric boundary layer. In: Wallace JM, Hobbs PV
835 (eds) *Atmospheric Science (Second Edition)*, second edition edn, Academic
836 Press, San Diego, pp 375–417
- 837 Stull RB (1988) An introduction to boundary layer meteorology, vol 13.
838 Springer Science & Business Media
- 839 Sullivan PP, McWilliams JC (2010) Dynamics of winds and currents coupled
840 to surface waves. *Annu Rev Fluid Mech* 42:19–42
- 841 Sweet M, Kocurek G (1990) An empirical model of aeolian dune lee-face air-
842 flow. *Sedimentology* 37:1023–1038
- 843 Sykes RI (1980) An asymptotic theory of incompressible turbulent boundary-
844 layer flow over a small hump. *J Fluid Mech* 101:647–670
- 845 Taylor P, Teunissen H (1987) The Askervein hill project: overview and back-
846 ground data. *Boundary-Layer Meteorol* 39:15–39
- 847 Taylor P, Mason P, Bradley E (1987) Boundary-layer flow over low hills.
848 *Boundary-Layer Meteorol* 39:107–132
- 849 Tsoar H, Yaalon DH (1983) Deflection of sand movement on a sinuous longi-
850 tudinal (seif) dune: use of fluorescent dye as tracer. *Sedimentary Geology*
851 36:25–39
- 852 Ungar JE, Haff PK (1987) Steady state saltation in air. *Sedimentology* 34:289–
853 299
- 854 Unsworth C, Parsons D, Hardy R, Reesink A, Best J, Ashworth P, Keevil G
855 (2018) The impact of nonequilibrium flow on the structure of turbulence
856 over river dunes. *Water Resour Res* 54:6566–6584
- 857 Uppala SM, Källberg P, Simmons AJ, Andrae U, Bechtold VDC, Fiorino M,
858 Gibson J, Haseler J, Hernandez A, Kelly G, et al. (2005) The era-40 re-
859 analysis. *Q J R Meteorol Soc* 131:2961–3012
- 860 Valance A, Rasmussen K, Ould El Moctar A, Dupont P (2015) The physics
861 of aeolian sand transport. *C R Phys* 16:1–13
- 862 Venditti JG, Best JL, Church M, Hardy RJ (2013) *Coherent Flow Structures*
863 at Earth's Surface. John Wiley & Sons
- 864 Virtanen P, Gommers R, Oliphant TE, Haberland M, Reddy T, Cournapeau
865 D, Burovski E, Peterson P, Weckesser W, Bright J, et al. (2020) Scipy 1.0:
866 fundamental algorithms for scientific computing in python. *Nature methods*
867 17:261–272
- 868 Vogelegang D, Holtslag A (1996) Evaluation and model impacts of alternative
869 boundary-layer height formulations. *Boundary-Layer Meteorol* 81:245–269
- 870 Vosper SB (2004) Inversion effects on mountain lee waves. *Q J R Meteorol Soc*
871 130:1723–1748
- 872 Walker I, Davidson-Arnott R, Bauer B, Hesp P, Delgado-Fernandez I, Oller-
873 head J, Smyth T (2017) Scale-dependent perspectives on the geomorphology
874 and evolution of beach-dune systems. *Earth-Science Review* 171:220–253
- 875 Walker IJ, Nickling WG (2002) Dynamics of secondary airflow and sediment
876 transport over and in the lee of transverse dunes. *Prog Phys Geogr* 26:47–75

- 877 Walker IJ, Hesp PA, Davidson-Arnott RG, Ollerhead J (2006) Topographic
878 steering of alongshore airflow over a vegetated foredune: Greenwich dunes,
879 prince edward island, canada. *Journal of Coastal Research* 22:1278–1291
- 880 Walker IJ, Hesp PA, Davidson-Arnott RG, Bauer BO, Namikas SL, Ollerhead
881 J (2009) Responses of three-dimensional flow to variations in the angle of
882 incident wind and profile form of dunes: Greenwich dunes, prince edward
883 island, canada. *Geomorphology* 105:127–138
- 884 Walmsley JL, Salmon J, Taylor P (1982) On the application of a model of
885 boundary-layer flow over low hills to real terrain. *Boundary-Layer Meteorol*
886 23:17–46
- 887 Weaver C, Wiggs G (2011) Field measurements of mean and turbulent airflow
888 over a barchan sand dune. *Geomorphology* 128:32–41
- 889 Werner BT, Kocurek G (1999) Bedform spacing from defect dynamics. *Geol-*
890 *ogy* 27:727–730
- 891 Wiggs G, Bullard J, Garvey B, Castro I (2002) Interactions between airflow
892 and valley topography with implications for aeolian sediment transport.
893 *Physical Geography* 23:366–380
- 894 Wood N (2000) Wind flow over complex terrain: a historical perspective and
895 the prospect for large-eddy modelling. *Boundary-Layer Meteorol* 96:11–32
- 896 Zhang C, Li Q, Zhou N, Zhang J, Kang L, Shen Y, Jia W (2016) Field obser-
897 vations of wind profiles and sand fluxes above the windward slope of a sand
898 dune before and after the establishment of semi-buried straw checkerboard
899 barriers. *Aeolian Res* 20:59–70
- 900 Zilker DP, Hanratty TJ (1979) Influence of the amplitude of a solid wavy wall
901 on a turbulent flow. part 2. separated flows. *J Fluid Mech* 90:257–271
- 902 Zilker DP, Cook GW, Hanratty TJ (1977) Influence of the amplitude of a solid
903 wavy wall on a turbulent flow. part 1. non-separated flows. *J Fluid Mech*
904 82:29–51

905 **Local wind regime induced by giant linear dunes**
 906 — Supplementary Material —

907 **C. Gadal* · P. Delorme · C. Narteau · G.F.S. Wiggs · M. Baddock ·**
 908 **J.M. Nield · P. Claudin**

909
 910 * Institut de Mécanique des Fluides de Toulouse, Université de Toulouse Paul
 911 Sabatier, CNRS, Toulouse INP-ENSEEIHT, Toulouse, France.
 912 cyril.gadal@imft.fr

913 **1. Shear velocity and calibration of the hydrodynamical roughness**

914 As the regionally predicted and locally measured velocities are available at
 915 different heights, we can not compare them directly. We therefore convert all
 916 velocities into shear velocities u_* , characteristic ~~of the turbulent~~ ~~the turbulent~~
 917 logarithmic velocity profile (Spalding 1961; Stull 1988):

$$\frac{u(z)}{u_*} = \frac{1}{\kappa} \ln \left(\frac{z}{z_0} \right), \quad (15)$$

918 where z is the vertical coordinate, $\kappa = 0.4$ the von Kármán constant and z_0 the
 919 hydrodynamic roughness. Note that, strickly speaking, this logarithmic profile
 920 is valid for a neutrally stratified ABL only. Vertical density gradients occuring
 921 in other conditions may thus induce large discrepancies (Monin and Obukhov 1954; Garratt 1994; Dyer 1974)
 922 . However, as our wind measurements are in the flow region close enough to
 923 the surface, where these effects are negligible, this logarithmic wind profile
 924 remains a fairly good approximation in all conditions (Gunn et al. 2021b).
 925 Several measurements of hydrodynamic roughnesses are available (Raupach
 926 1992; Bauer et al. 1992; Brown et al. 2008; Nield et al. 2014). In the absence
 927 of sediment transport, it is governed by the geometric features of the bed
 928 (Flack and Schultz 2010; Pelletier and Field 2016). When aeolian saltation
 929 occurs, it is rather controlled by the altitude of Bagnold's focal point (Durán
 930 et al. 2011; Valance et al. 2015), which depends on the wind velocity and grain
 931 properties (Sherman and Farrell 2008; Zhang et al. 2016; Field and Pelletier
 932 2018). Whether associated with geometric features or with sediment transport,
 933 its typical order of magnitude is the millimetre scale on sandy surfaces.

934 We do not have precise velocity vertical profiles to be able to deduce an
 935 accurate value of z_0 in the various environments of the meteorological stations
 936 (vegetated, arid, sandy). Our approach is to rather select the hydrodynamic
 937 roughness which allows for the best possible matching between the regionally
 938 predicted and locally measured winds, i.e. minimising the relative difference δ
 939 between the wind vectors of both datasets:

$$\delta = \frac{\sqrt{\langle \| \mathbf{u}_{*,\text{era}} - \mathbf{u}_{*,\text{station}} \|^2 \rangle}}{\sqrt{\langle \| \mathbf{u}_{*,\text{era}} \|^2 \rangle \langle \| \mathbf{u}_{*,\text{station}} \|^2 \rangle}}, \quad (16)$$

where $\langle \cdot \rangle$ denotes time average. This parameter is computed for values of z_0 in ERA5-Land analysis ranging from 10^{-5} m to 10^{-2} m for the four different stations. Note that for the North Sand Sea and South Sand Sea stations, where the giant dunes feedback presumably affect the wind, we take into account the non-deflected winds only in the calculation of δ (with a 15° tolerance).

As shown in Online Resource Fig. S3, the minimum values of δ in the space $(z_0^{\text{ERA5Land}}, z_0^{\text{local}})$ form a line. We thus set the roughness in the ERA5-Land analysis to the typical value $z_0 = 10^{-3}$ m, and deduce the corresponding ones for the local stations. It leads to 2.7, 0.8, 0.1 and 0.5 mm for the Etosha West, North Sand Sea, Huab and South Sand Sea stations, respectively. Importantly, this approach somewhat impacts the calculation of the shear velocities, but not that of the wind directions. As such, most of our conclusions are independent of such a choice. However, it may affect the magnitude of the wind velocity attenuation/amplification in flow confinement situations.

2. Computation of the ABL characteristics

The estimation of the non-dimensional numbers associated with the ABL requires the computation of representative meteorological quantities. In arid areas, the vertical structure of the atmosphere can be approximated by a well mixed convective boundary layer of height H , topped by the stratified free atmosphere (Stull 1988; Shao 2008). In this context, one usually introduces the virtual potential temperature T_{vp} , which is a constant T_0 inside the boundary layer, and increases linearly in the FA (Online Resource Fig. S8a):

$$T_{\text{vp}}(z) = \begin{cases} T_0 & \text{for } z \leq H, \\ T_0 \left(1 + \frac{\Delta T_{\text{vp}}}{T_0} + \frac{N^2}{g}(z - H) \right) & \text{for } z \geq H, \end{cases} \quad (17)$$

where ΔT_{vp} is the temperature discontinuity at the capping layer and $N = \sqrt{g\partial_z T_{\text{vp}}/T_0}$ is the Brunt-Väisälä frequency, characteristic of the stratification. Note that, under the usual Boussinesq approximation, temperature and air density variations are simply related by $\delta T_{\text{vp}}/T_0 \simeq -\delta\rho/\rho_0$ (see Online Resource of Andreotti et al. (2009)), so that N can equivalently be defined from the density gradient as next to (1).

The ERA5 dataset provides vertical profiles of the geopotential ϕ , the actual temperature T and the specific humidity η at given pressure levels P . The vertical coordinate is then calculated as:

$$z = \frac{\phi R_t}{g R_t - \phi}, \quad (18)$$

where $R_t = 6371229$ m is the reference Earth radius and $g = 9.81$ m s $^{-2}$ is the gravitational acceleration. One also computes the virtual potential temperature as:

$$T_{\text{vp}} = T \left[1 + \left(\frac{M_d}{M_w} - 1 \right) \eta \right] \left(\frac{P_0}{P} \right)^{R/C_p}, \quad (19)$$

where $P_0 = 10^5$ Pa is the standard pressure, $R = 8.31$ J/K is the ideal gas constant, $C_p \simeq 29.1$ J/K is the air molar heat capacity, and $M_w = 0.018$ kg/Mol and $M_d = 0.029$ kg/Mol are the molecular masses of water and dry air respectively. The specific humidity is related to the vapour pressure p_w as

$$\eta = \frac{\frac{M_w}{M_d} p_w}{p - \left(1 - \frac{M_w}{M_d}\right) p_w}. \quad (20)$$

The ERA5 dataset also provides an estimate of the ABL depth H , based on the behaviour of the Richardson vertical profile. This dimensionless number is defined as the ratio of buoyancy and flow shear terms, and can be expressed as $\text{Ri} = N^2 / (\partial_z u)^2$. It vanishes in the lower well-mixed layer where T_{vp} is constant, and increases in the stratified FA. Following the method and calibration of Vogelegang and Holtlag (1996); Seidel et al. (2012), the value $\text{Ri}(z) \simeq 0.25$ has been shown to be a good empirical criterion to give $z \simeq H$ within a precision varying from 50% for the shallower ABL (e.g. at night) to 20% for situations of stronger convection.

Examples of vertical profiles of the virtual potential temperature deduced from ERA5 are shown in Online Resource Fig. S8a. For each of them, an average temperature is computed below the ABL depth ($z < H$), and a linear function is fitted above, allowing us to extract the temperature jump ΔT_{vp} . Importantly, some profiles display a vertical structure that cannot be approximated by the simple form (17) used here (Online Resource Fig. S8b). In practice, we removed from the analysis all of those leading to the unphysical case $\Delta T_{\text{vp}} < 0$. We have noticed that these ‘ill-processed’ profiles dominantly occur in winter and are evenly spread across the hours of the day. Importantly, they represent $\simeq 12\%$ of the data only (Online Resource Fig. S8c,d), and we are thus confident that this data treatment does not affect our conclusions.

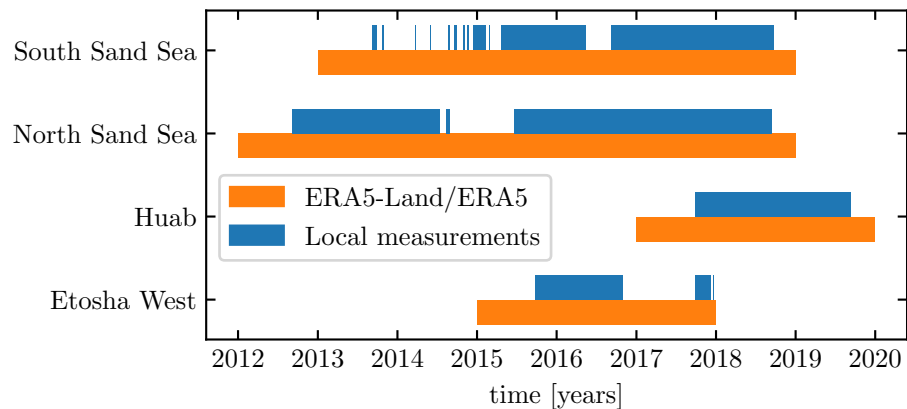


Fig. S1 Gant chart representing the valid time steps for the two data sets, for all stations.

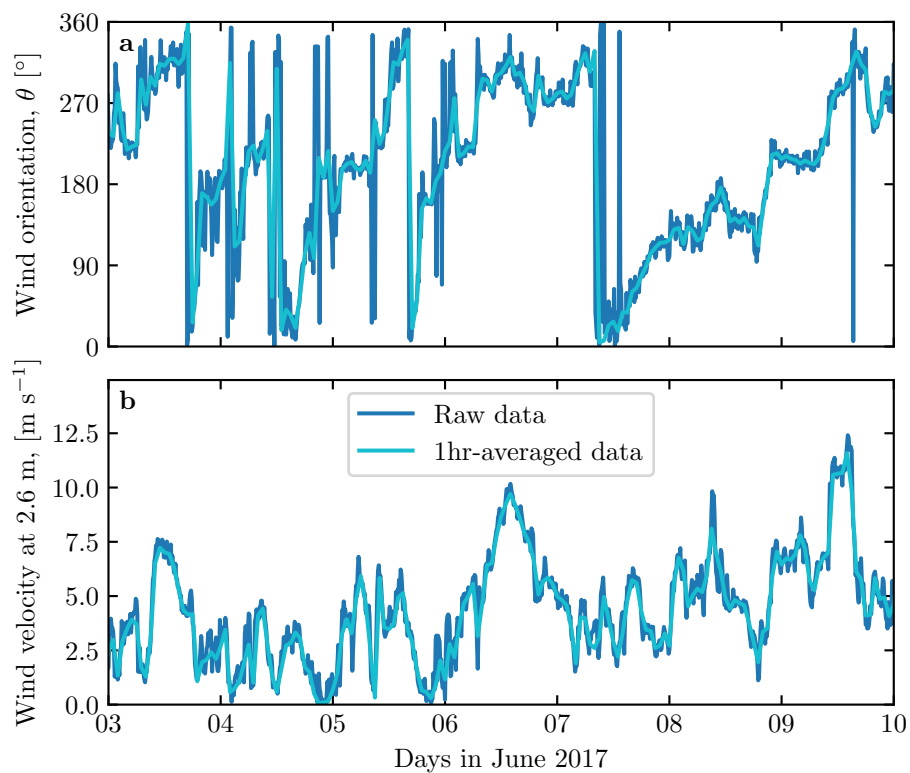


Fig. S2 Comparison between raw local and hourly-averaged wind measurements for South Sand Sea station. **a:** wind direction. **b:** wind velocity at height 2.6 m.

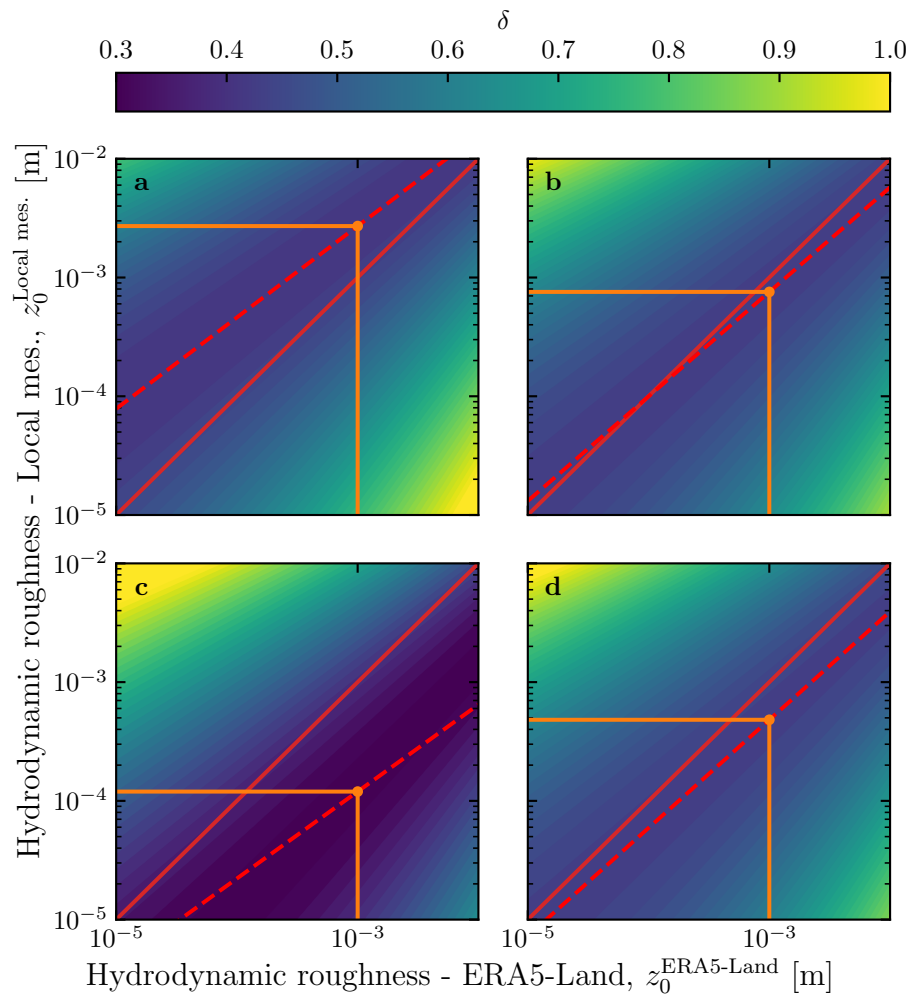


Fig. S3 Calibration of hydrodynamic roughness. The parameter δ (16) quantifying the difference between local and predicted winds is shown as a function of the hydrodynamic roughnesses chosen for the ERA5-Land and for local winds, for the (a) Etosha West, (b) North Sand Sea, (c) Huab and (d) South Sand Sea stations. The red dashed and plain lines show the minima of δ and the identity line, respectively. The orange lines and dots highlight the chosen hydrodynamic roughnesses for the local winds deduced from setting $z_0^{\text{ERA5Land}} = 1 \text{ mm}$.

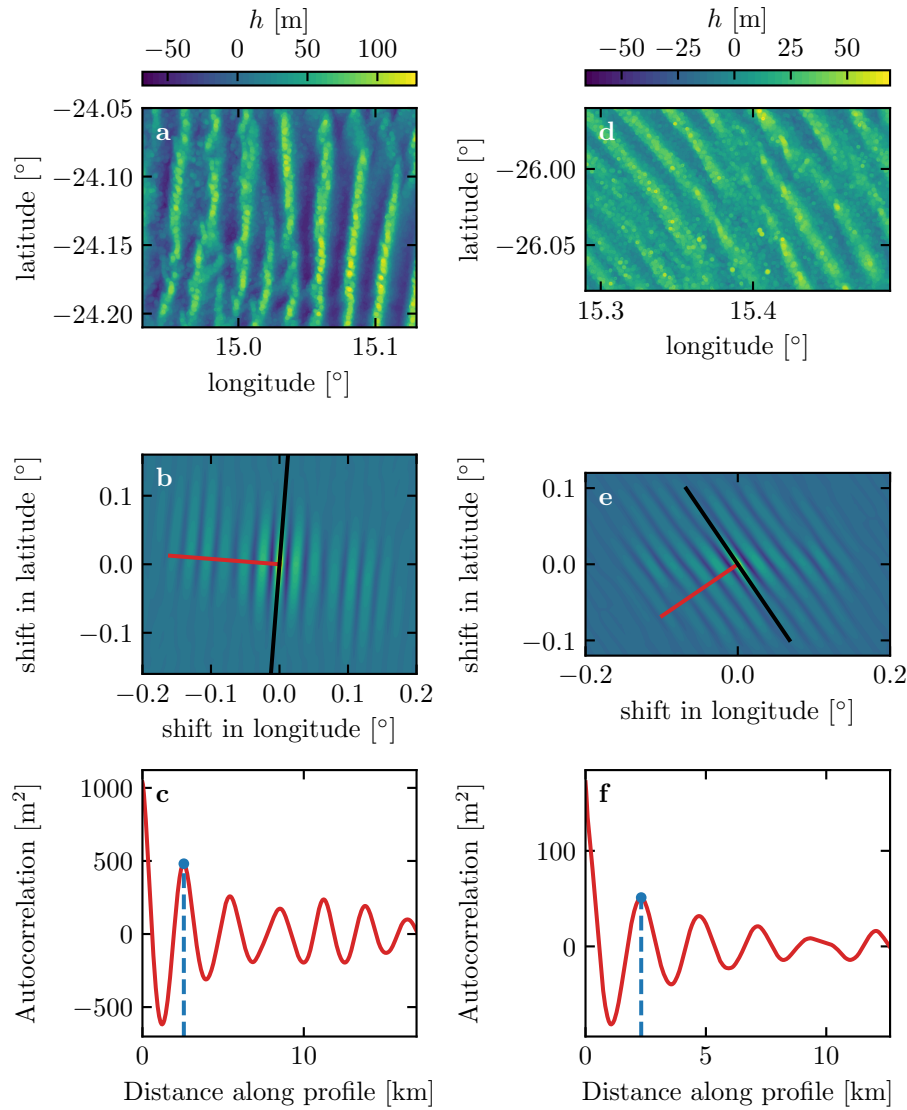


Fig. S4 Analysis of the DEMs of the North Sand Sea (left column – panels **a**, **b**, **c**) and South Sand Sea (right column – panels **d**, **e**, **f**) stations. **a–d**: Bed elevation detrended by a fitted second order polynomial base-line. **b–e**: Autocorrelation matrix shown in [color scale](#). The black line shows the detected dune orientation, and the red line represents the autocorrelation profile along which the dune wavelength is calculated, displayed in **c–f**. The blue lines and dots show the first peak of the autocorrelation profile, whose abscissa gives the characteristic wavelength of the dune pattern.

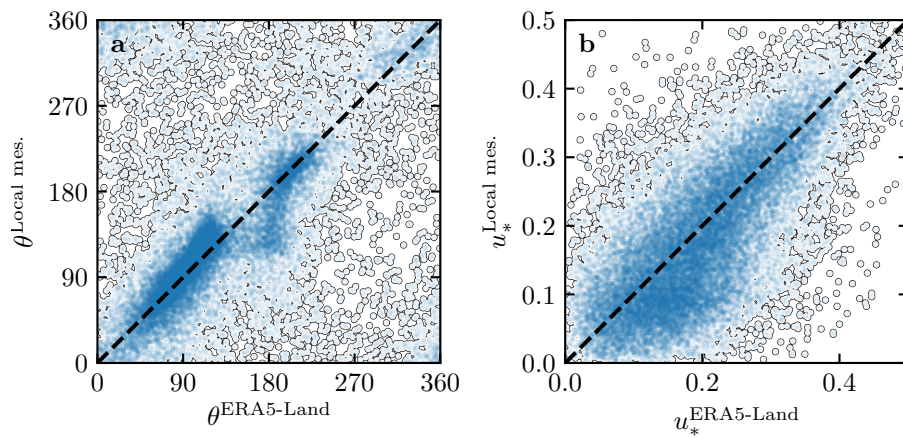


Fig. S5 Statistical comparison of the wind orientation (a) and velocity (b) between the ERA5-Land dataset and the local measurements for the Huab and Etosha West stations. Data point clustering around identity lines (dashed and black) provide evidence for agreement of the two sets.

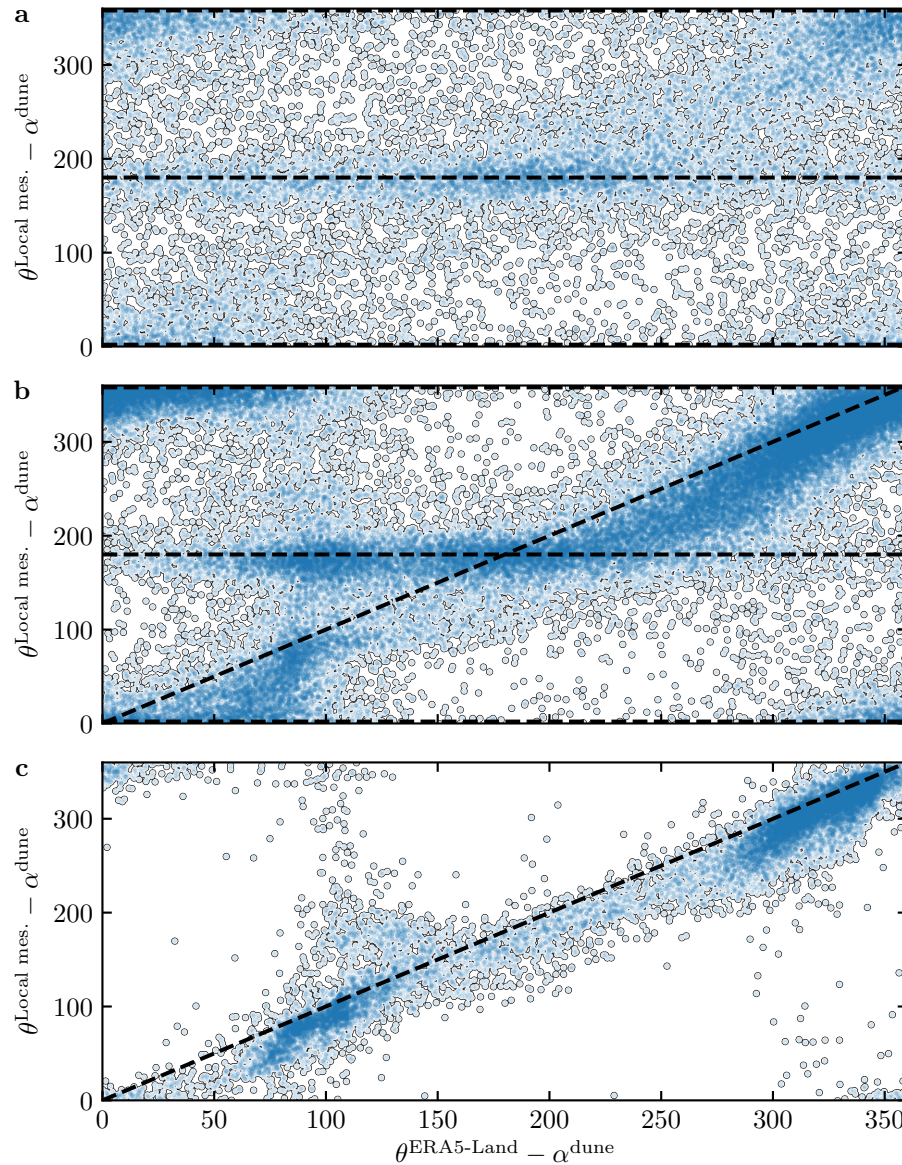


Fig. S6 Statistical comparison of the wind orientation between the ERA5-Land dataset and the local measurements for the South Sand Sea and North Sand Sea stations, for different velocity ranges. **a:** $u_{*,\text{ERA}} < 0.1 \text{ m s}^{-1}$ $u_{*,\text{ERA5-Land}} < 0.1 \text{ m s}^{-1}$. **b:** $0.1 < u_{*,\text{ERA}} < 0.25 \text{ m s}^{-1}$ $0.1 < u_{*,\text{ERA5-Land}} < 0.25 \text{ m s}^{-1}$. **c:** $u_{*,\text{ERA}} > 0.25 \text{ m s}^{-1}$ $u_{*,\text{ERA5-Land}} > 0.25 \text{ m s}^{-1}$. The measured dune orientations are subtracted to the wind orientation, which allows us to plot both stations on the same graph. Black dashed lines indicate locally measured orientations aligned with the dune crests (here 0°, 180° and 360° – panels **a**, **b**), as well as the identity lines (panels **b**, **c**).

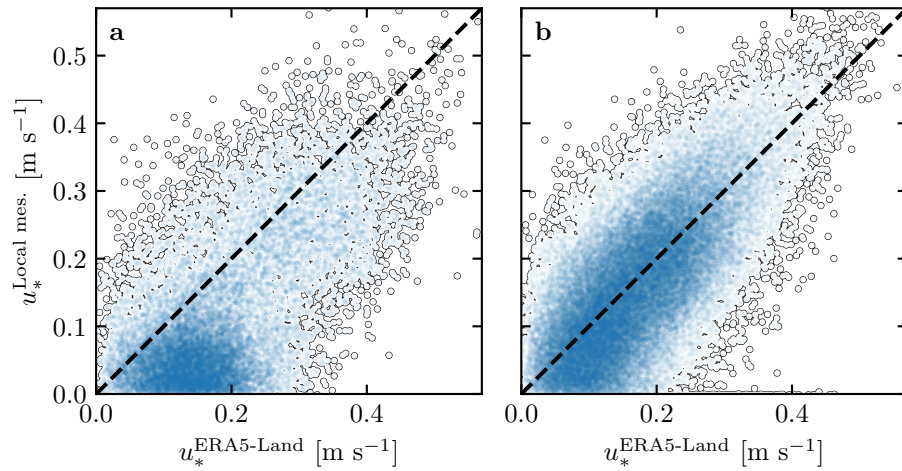


Fig. S7 Statistical comparison of the wind velocity between the ERA5-Land dataset and the local measurements for the South Sand Sea and North Sand Sea stations. **a:** Nocturnal summer easterly wind. **b:** Diurnal southerly wind. Black dashed lines are identity lines. The angle ranges used to select diurnal and nocturnal summer winds are the same as those in Figs. 4 and Figs. 6 of the main article.

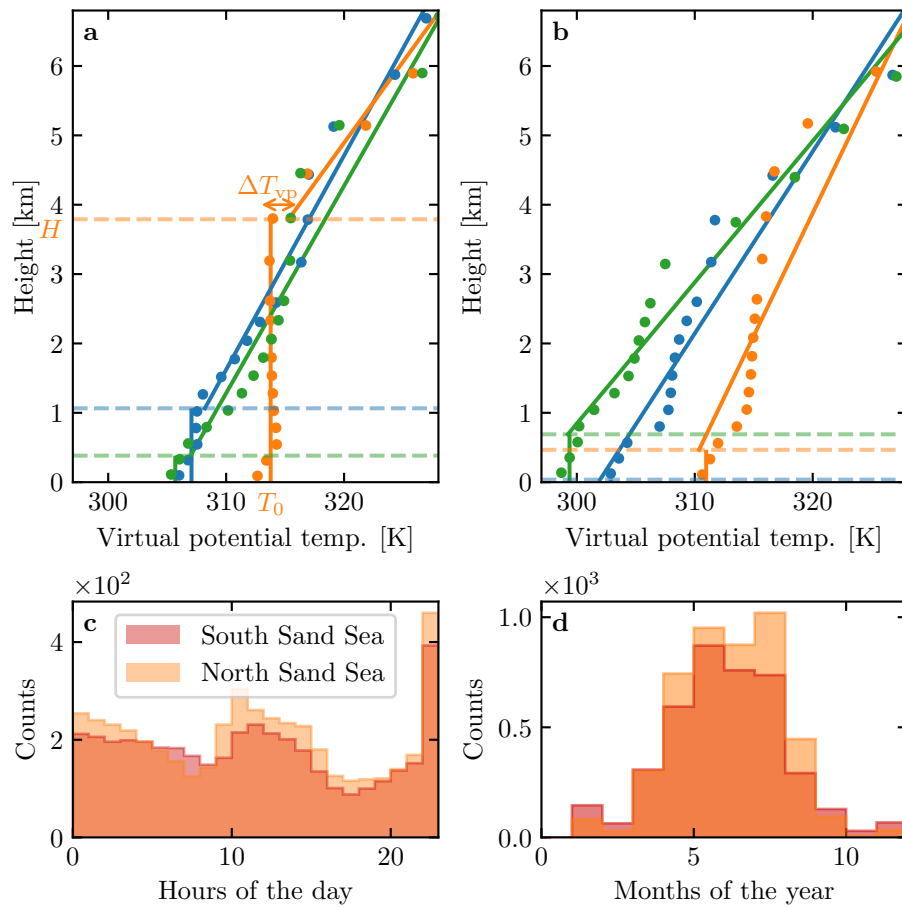


Fig. S8 **a:** Vertical profiles of the virtual potential temperature at three different times (blue: 29/11/2012 - 11:00–11:00 UTC, orange: 21/03/2017 - 12:00–12:00 UTC, green: 21/03/2017 - 20:00–20:00 UTC) at the South Sand Sea station. Dots: data from the ERA5 reanalysis. Dashed lines: boundary layer height given by the ERA5 reanalysis. Plain lines: vertical (ABL) and linear (FA) fits to estimate the quantities displayed in Online Resource Fig. S9. **b:** Examples of ill-processed vertical profiles at three different times (blue: 2/12/2013 - 23:00–23:00 UTC, orange: 20/03/2017 - 00:00–00:00 UTC, green: 14/07/2017 - 14:00–14:00 UTC) at the South Sand Sea station. **c:** Hourly distribution Distribution of ill-processed vertical profiles at South (orange) and North (light orange) Sand Sea station: Monthly distribution of ill-processed vertical profiles hourly (c) and monthly (d) counts.

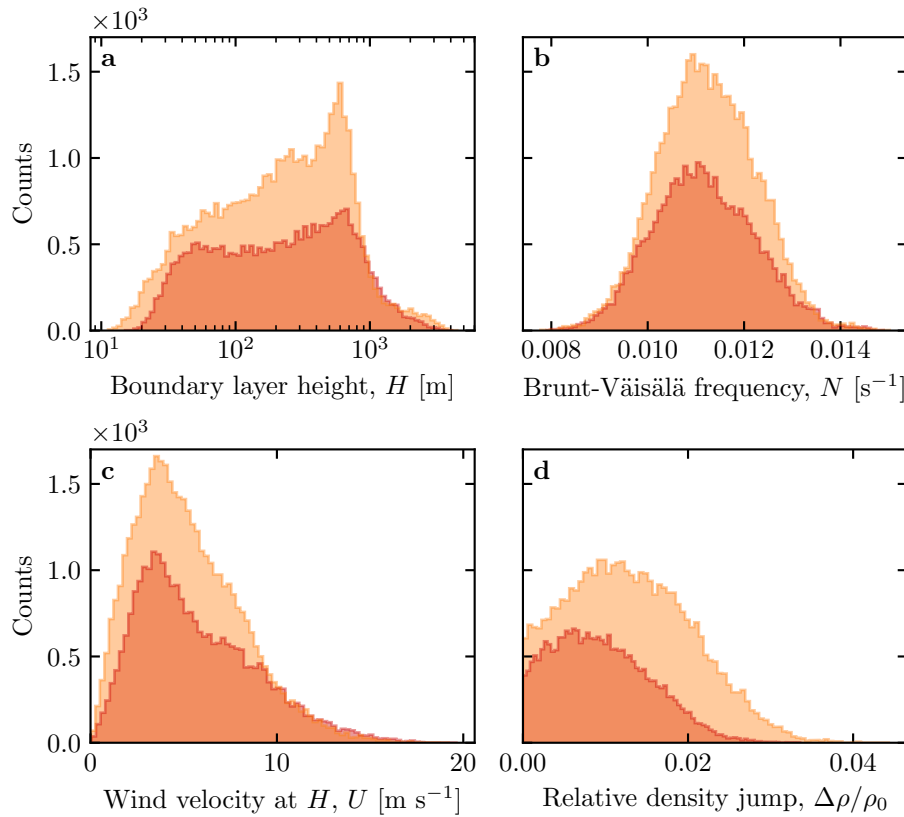


Fig. S9 Distributions of the meteorological parameters resulting from the processing of the ERA5-Land data for the South Sand Sea (blue/orange) and the North Sand Sea (light orange) stations.

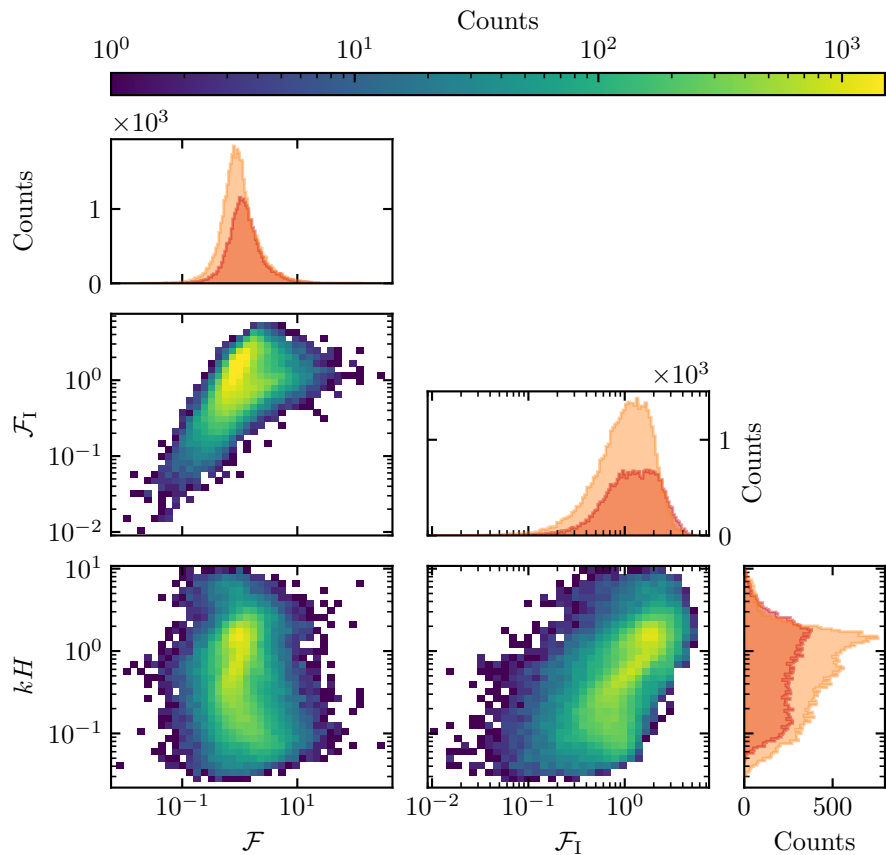


Fig. S10 Non-dimensional parameters distributions. For the marginal distributions, the light orange corresponds to the South Sand Sea station, and the blue to the North Sand Sea station.

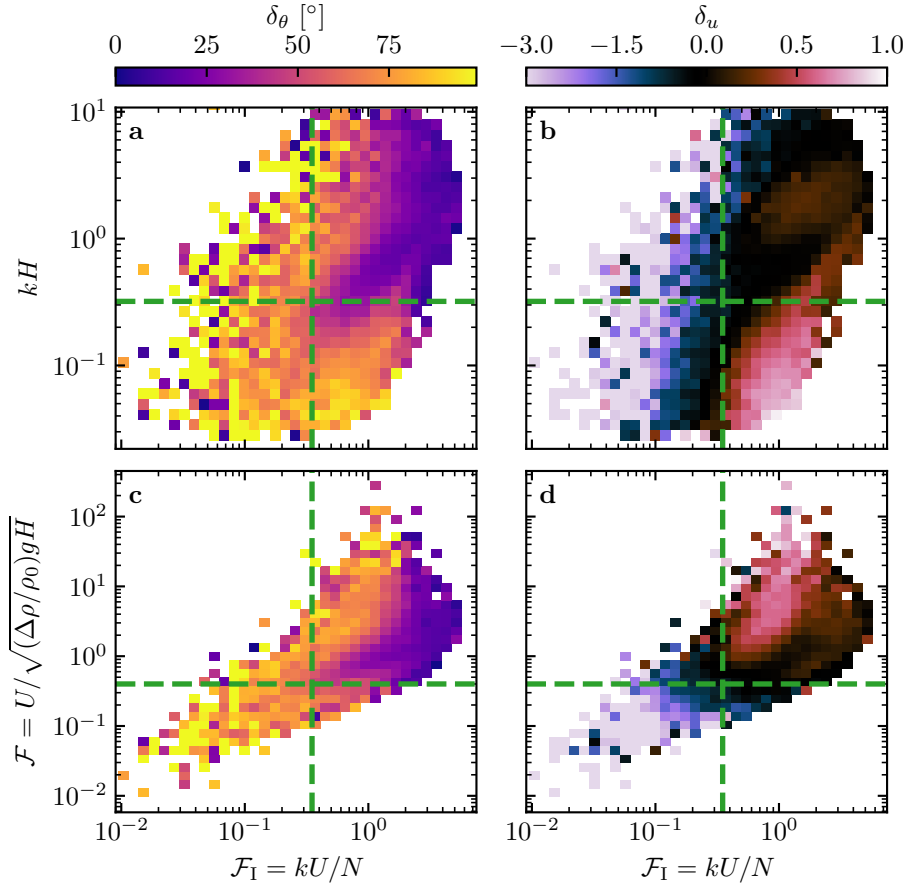


Fig. S11 Regime diagrams of the wind deviation δ_θ and relative attenuation/amplification δ_u in the spaces (\mathcal{F}_I, kH) and $(\mathcal{F}_I, \mathcal{F})$, containing the data from both the North Sand Sea and South Sand Sea stations. Green dashed lines empirically delimit the different regimes. The point density in each bin of the diagrams is shown in Online Resource Fig. S10 – 95% of the data occur in the range $-1 < \delta u < 1$. The similar regime diagrams in the space (\mathcal{F}, kH) are shown in Fig. 8.

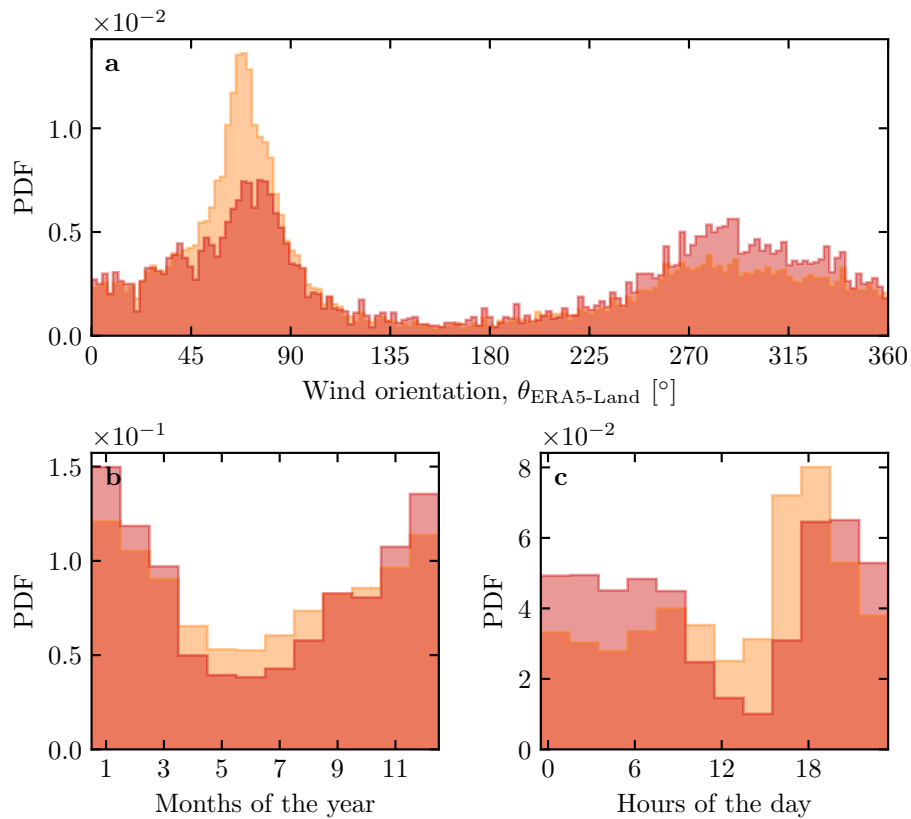


Fig. S12 Normalized distributions of amplified velocities for the North sand Sea (blue light , orange: $\delta_u < 0$, orange: $\delta_u < -0.5$). **a:** Angular distributions. **b:** Monthly distributions. **c:** Hourly distributions.

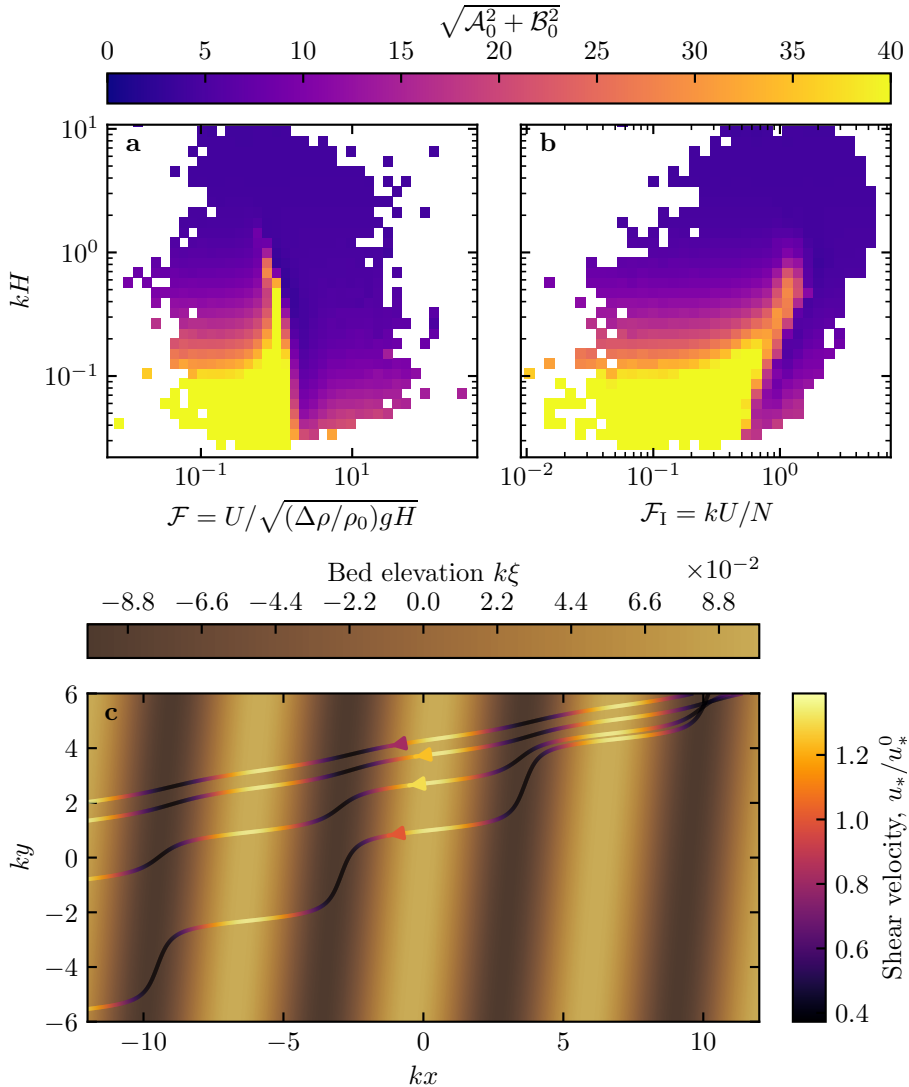


Fig. S13 Computation of the flow disturbance with the linear model of Andreotti et al. (2009). **a–b:** Magnitude of the hydrodynamic coefficients A_0 and B_0 , calculated from the time series of the non-dimensional numbers corresponding to the ERA5-Land wind data and ERA5 data on vertical pressure levels. **c** Shear velocity streamlines over sinusoidal ridges of amplitude $k\xi_0 = 0.1$ and for increasing values of $\sqrt{A_0^2 + B_0^2}$. From the upper to the lower streamline, values of $(kH, F, F_I, A_0, B_0, \sqrt{A_0^2 + B_0^2})$ are $(1.9, 0.6, 1.5, 3.4, 1.0, 3.5)$, $(1.5, 0.3, 0.4, 4.8, 1.4, 5.0)$, $(0.1, 3.5, 1.0, 8.6, 0.1, 8.6)$, $(0.5, 0.05, 0.04, 9.6, 2.5, 9.9)$.

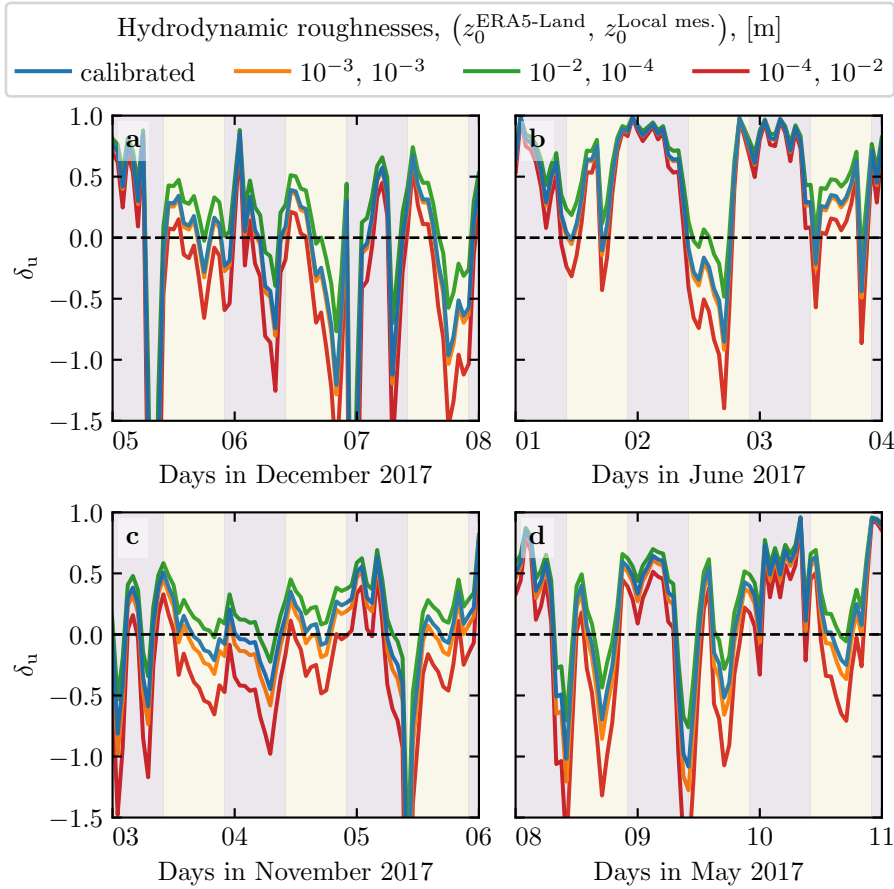


Fig. S14 Time series of the relative velocity disturbance δ_u corresponding to Fig. 5, for different values of the hydrodynamic roughnesses. **a:** North Sand Sea summer, **b:** North Sand Sea winter, **c:** South Sand Sea summer, **d:** South Sand Sea winter. Note that δ_u is independent of the choice of z_0^{Era5Land} , $z_0^{\text{ERA5-Land}}$ and z_0^{local} , $z_0^{\text{Local mes.}}$.